Pressure Adaptive Bellows

A Concept for Variable Stiffness and Variable Camber

Dennis van Dommelen

Technische Universiteit Delft

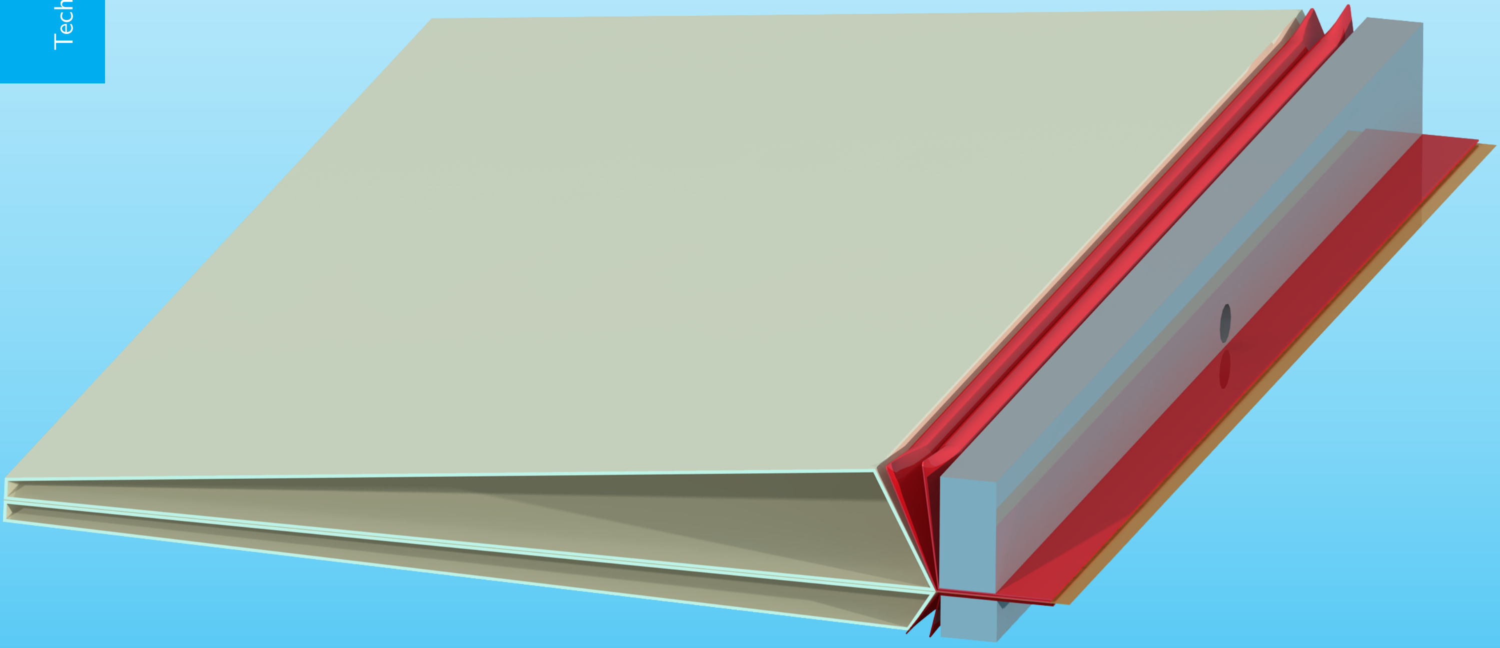

Delft University of Technology

Challenge the future

PRESSURE ADAPTIVE BELLOWS

A CONCEPT FOR VARIABLE STIFFNESS AND VARIABLE CAMBER

by

Dennis van Dommelen

in partial fulfillment of the requirements for the degree of

Master of Science
in Aerospace Engineering

at the Delft University of Technology,
to be defended publicly on Tuesday April 11, 2017 at 13:00.

Thesis registration number:	153#17#MT#FPP	
Supervisor:	Dr. ir. R. Vos	
Thesis committee:	Prof. dr. ir. L. L. M. Veldhuis,	TU Delft
	Dr. ir. R. De Breuker,	TU Delft
	Prof. Dr. R. M. Barrett,	The University of Kansas

Delft
University of
Technology

TUDelft Delft University of Technology

DELFT UNIVERSITY OF TECHNOLOGY
DEPARTMENT OF
FLIGHT PERFORMANCE AND PROPULSION

The undersigned hereby certify that they have read and recommend to the Faculty of Aerospace Engineering for acceptance a thesis entitled **“Pressure Adaptive Bellows: A Concept for Variable Stiffness and Variable Camber”** by **Dennis van Dommelen** in partial fulfillment of the requirements for the degree of **Master of Science**.

Dated: April 11, 2017

Head of department:

Prof. dr. ir. L. L. M. Veldhuis

Supervisor:

Dr. ir. R. Vos

Reader:

Dr. ir. R. De Breuker

Reader:

Dr. R. M. Barrett

PREFACE

In December 2014, I made the decision to do my internship at DARcorporation in Lawrence, KS. Almost a year later, at the end of my internship I got in touch with Dr. Ron Barrett and started talking about ideas for doing a master thesis at The University of Kansas. He got me very enthusiastic about continuing Dr. ir. Roelof Vos' PhD research and looking for practical applications of this concept. Dr. ir. Roelof Vos induced variable camber by using a pressure adaptive honeycomb structure. After consulting Roelof Vos himself to be my supervisor, it was all set to go.

I started very enthusiastically with the literature study in April 2016. The intended goal was to apply the pressure adaptive structure to a business jet wing. Together with Ron Barrett, I took a trip down to Dodson Airplane junkyard in Rantoul, KS to investigate some business jet parts. We found a Cessna Citation X inboard flap, however Dodson was not very eager to lend this flap to The University of Kansas and the purchase would be out of the budget. Luckily Ron Barrett and Willem Anemaat (President at DARcorporation) knew Albert Dirkzwager at Textron Aviation, they had a flap which was used for structural testing. So Ron and I made the trip down to Wichita, KS to pick up the inboard flap. This was a very interesting experience and we retrieved this expensive aircraft part. Due to the structural testing, the flap had test pads attached to them and they purposely made two cutouts to the trailing edge to weaken the structure. Removing the test pads took a while and after that I prepared the flap for molding and created the molds.

Since I would be in Kansas for eight months to finish the project, the practical work had to be finished before I returned to the Netherlands. Because of time constraints I did not succeed in fulfilling my intentions. My intention was to produce and test (structurally and aerodynamically) a full scale business jet flap with the pressure adaptive actuation to the trailing edge. More towards the end of the project it was decided to test the structural behavior of one of the actuators instead of the complete flap. It is unsatisfactory to not get the project at the level you wanted it to be and it is difficult to test it when there are still imperfections in the actuator due to manual production techniques. However I can still say the produced actuator looks promising and I do really hope this idea is not going to disappear on the shelf for years.

I would like to thank The University of Kansas, Textron Aviation, Ron Barrett as supervisor of The University of Kansas, and Roelof Vos, as supervisor from the Technical University of Delft, for granting me this opportunity and the support during the project. They gave me the opportunity to work in a different research environment and meet a lot of professional aerospace engineers. It also gave me the opportunity to work part time at DARcorporation. This made the workweek very intense with a lot of working hours, however it gave me valuable experience and a starting position after graduation. Especially the weeks before returning to The Netherlands were very intense, where it was not unusual to work over sixty hours a week divided over all seven days. This was only possible by the support I got from my parents, friends, roommates and the soccer teams I was on. They gave me the right amount of distractions to not lose overview and productivity along the way.

Dennis van Dommelen
Delft, March 2017

SUMMARY

The introduction of metal into the aeronautical industry made the wings and aerostructures stiff and rigid. High-lift devices and movable surfaces allow for discrete deflections to increase lift coefficient and control of the aircraft. Several researchers have proposed concepts for variable camber, allowing continuous deflections. This is achieved by shape memory alloys, piezoelectric actuators, fishbone structures and pressure adaptive actuation. The concept of variable stiffness is not applied in aviation nowadays. This thesis is focused on applying variable camber and variable stiffness to a Cessna Citation X inboard flap, for which a full scale actuator is produced and tested.

The loads are estimated on the inboard flap with the morphing part in neutral, 15 degrees downwards and 15 degrees upwards position. The maximum loads and moments are found in the descent flight condition, which equal 209.7 N and 15.24 $N \cdot m$ in neutral position. Deflection downwards increases the force and moment to 631.6 N and 37.19 $N \cdot m$, whereas in upwards position the force and moment equal -253.4 N and -12.68 $N \cdot m$.

With the expected loads on the trailing edge of the flap, the actuator can be designed. The top bellows are designed 2.62 times larger than the bottom bellows, because of the expected loading ratio. The wedge angles are approximately 30 degrees, which are the maximum angles for deflection in positive and negative direction. The bellows and trailing edge are made from polycarbonate, where the bellows and the inner sheet of the trailing edge have a thickness of 4 mil (0.10 mm) and 6.7 mil (0.17 mm). The trailing edge is made from 30 mil (0.762 mm) polycarbonate sheet. The stringers are replaced by aluminum spars for the test setup. The main issue found in the testing phase, was the air tightness. Even though the bellows were not completely airtight, the bellows could be inflated by applying 10 psi (0.69 bar) air pressure.

In the testing phase, the maximum deflections and deflection speeds have been measured. On average 13 degrees upwards deflection and 7 degrees downward deflection is reached. The actuation speed equals 150 deg/s and deflection rates range from 0.88 Hz to 3.33 Hz.

The stiffness and damping have been determined as well. The stiffness increases with air pressure, for a 4 mil inner sheet thickness the stiffness increases from 3.46 $N \cdot m/rad$ to 5.38 $N \cdot m/rad$, the 6.7 mil inner sheet increases more, from 3.96 $N \cdot m/rad$ to 9.03 $N \cdot m/rad$. It is expected that the stiffness can be varied linearly between the neutral and inflated (10 psi) state. A thicker inner sheet gives a higher stiffness.

The damping coefficients are only determined for the 4 mil inner sheet. The damping coefficients equal 0.119 in deflated, 0.143 in neutral and 0.226 in inflated condition. The natural frequency could be determined from the damping test as well. The natural frequency was approximately 2.99 Hz for the deflated and the neutral tests and 3.71 Hz for the inflated tests. The equivalent torsional stiffness corresponding to this natural frequency equals 1.21 $N \cdot m/rad$, 1.24 $N \cdot m/rad$ and 1.88 $N \cdot m/rad$ for the deflated, neutral and inflated tests respectively.

The stiffness and damping coefficients are used in a torsional spring damper differential equation, together with the mass moment of inertia for the trailing edge, which is calculated in CATIA™. The mass moment of inertia equals 0.422 $g \cdot m^2$ for the 4 mil and 0.434 $g \cdot m^2$ for the 6.7 mil inner sheet. Another analytic model is created as well, determining the deflection from the final shape of the inflated bellows.

Since the actuator is still in an early development phase, it is expected that the actuator and analytic models can be improved with more research and better production techniques.

CONTENTS

Summary vii

List of Figures xi

List of Tables xiii

Nomenclature xvi

1 Introduction 1
- 1.1 Background Information on Variable Camber and Variable Stiffness . . . 1
- 1.2 The Cessna Citation X Inboard Flap . . . 4
- 1.3 Research Questions and Aims . . . 6

2 Lift Coefficient Analysis and Load Estimation 7
- 2.1 Aircraft Model and Lift Coefficient Analysis . . . 7
- 2.2 Neutral Morphing Load Estimation . . . 9
- 2.3 Positive Morphing Load Estimation . . . 11
- 2.4 Negative Morphing Load Estimation . . . 12
- 2.5 Effect of Morphing on Load Estimation . . . 13
- 2.6 V-n Diagram . . . 15
- 2.7 Expected Loading on the Morphing Part of the Flap . . . 15

3 Preliminary Design and Test Setup 17
- 3.1 Preliminary Design . . . 17
- 3.2 Bellow Design . . . 19
- 3.3 Trailing Edge Design . . . 21
- 3.4 Test Setup . . . 22

4 Production of the Actuator 25
- 4.1 Material . . . 25
  - 4.1.1 Polycarbonate . . . 25
  - 4.1.2 Aluminum . . . 25
  - 4.1.3 Kevlar® and Graphite Composites . . . 26
- 4.2 Parts . . . 26
  - 4.2.1 Bellows . . . 26
  - 4.2.2 Spar . . . 27
  - 4.2.3 Leading Edge . . . 27
  - 4.2.4 Trailing Edge . . . 27
- 4.3 Assembly . . . 28
- 4.4 Weight Measurement and Estimation . . . 30
- 4.5 Production and Testing Issues . . . 31
  - 4.5.1 Thickness Issues . . . 31
  - 4.5.2 Dimensional Issues . . . 32
  - 4.5.3 Adhesive Issues . . . 32
  - 4.5.4 Testing Issues . . . 33

5 Test results 35
- 5.1 Deflection . . . 35
- 5.2 Deflection rate . . . 36
- 5.3 Stiffness . . . 38
- 5.4 Damping . . . 42

6 Analytic Model for Stiffness and Deflection **45**
6.1 Stiffness Model 45
6.2 Deflection Model 46

7 Conclusions and Recommendations **49**
7.1 Conclusions to Sub Research Questions. 49
7.2 Recommendations on Further Research 50

Bibliography **53**

LIST OF FIGURES

1.1 FishBAC structure [8] . . . 2
1.2 AFC structure for an integrated truss design and a hinged design [14] . . . 2
1.3 Variable camber by PBP piezolectric actuation [20] . . . 3
1.4 Pressure adaptive honeycomb topology [26] . . . 3
1.5 Lift curves for a wind tunnel model in null position at a variety of BCDP [28] . . . 4
1.6 Bidirectional actuation scheme of PAH actuator [28] . . . 4
1.7 Cutaway of the Cessna Citation Excel wing [30] . . . 5
1.8 Measured thickness distributions and cambered profiles for Cessna Citation X inboard flap . . . 6

2.1 Airplane three view from Jane's All the World's Aircraft [29] compared to the AAA model (Red) . . 8
2.2 Spanwise lift distribution for different flight conditions for the Cessna Citation X from AAA with the inboard flap location highlighted . . . 8
2.3 Pressure distributions for different flight conditions, morphing part neutral as analyzed in XFOIL with the flight conditions as given in Table 2.1 . . . 9
2.4 Pressure distributions stalled MS(1)-0313 airfoil, analyzed in XFOIL with $Re = 29.9 \cdot 10^6$ . . . 10
2.5 Pressure distributions for different flight conditions, morphing part deflected +15 degrees analyzed in XFOIL with the flight conditions given in Table 2.1 . . . 11
2.6 Pressure distributions for different flight conditions, morphing part deflected -15 degrees analyzed in XFOIL with the flight conditions given in Table 2.1 . . . 12
2.7 Pressure distributions from XFOIL for descent condition, morphing part Neutral (N), 15 degrees Down (D) and 15 degrees Up (U) position, $c_l = 0.17$, $Re = 29.9 \cdot 10^6$, $M = [0.6, 0.3, 0.6]$ respectively 14
2.8 Pressure distributions from XFOIL for approach condition, morphing part Neutral (N), 15 degrees Down (D) and 15 degrees Up (U) position, $c_l = 0.594$, $Re = 16.8 \cdot 10^6$, $M = 0.197$ . . . 14
2.9 Pressure distribution from XFOIL for continuous and discrete deflection, $c_l = 1$, $Re = 16.8 \cdot 10^6$, $M = 0.197$ . . . 15
2.10 V-n diagram for Cessna Citation X from AAA . . . 15

3.1 Preliminary bellow layout structure inside the flap with the bellows in red and the flap skin in brown showing approximately the trailing 50% of the flap . . . 17
3.2 Actuator functionality explained, deflection with pressure p_a and $p_a + \Delta p$ and increasing the stiffness to $\kappa + \Delta\kappa$, the trailing edge (yellow) is only partially shown . . . 18
3.3 Preliminary design inside the flap with the bellows in red, L-stringers in grey, trailing edge in yellow and the flap skin in light blue . . . 18
3.4 Preliminary design inside the flap showing approximately the trailing 35% of the chord, with the bellows in red, L-stringers in grey, trailing edge in yellow and the flap skin in light blue . . . 19
3.5 Top and section view of the actuator with dimensions in [mm] and [deg] . . . 19
3.6 Top view of the preliminary design of the top bellows with dimensions in [mm] and [deg] . . . 20
3.7 Cross-sectional view of the preliminary design of the top bellows with dimensions in [mm] and [deg] . . . 20
3.8 Top view of the preliminary design of the bottom bellows with dimensions in [mm] and [deg] . 20
3.9 Cross-sectional view of the preliminary design of the bottom bellows with dimensions in [mm] and [deg] . . . 21
3.10 Front and side view of the top part of the trailing edge with dimensions in [mm] and [deg] . . . 21
3.11 Front and side view of the top part of the trailing edge with dimensions in [mm] and [deg] . . . 22
3.12 Maximum deflection due to wedge geometry visualized, maximum positive deflection in blue, maximum negative deflection in red . . . 22
3.13 Rendering of the test object with the bellows in red, spars in grey, trailing edge in yellow and the inner sheet in black . . . 23

3.14 Rendering of the test setup where the test object from Figure 3.13 is mounted on top of the green test stand . . . 23

4.1 Production processes of the bellows . . . 27
4.2 Top of the trailing edge with order of the corners in which they are formed by the press . . . 28
4.3 Layers of the bellows which need to be cut (numbered) and location where adhesive has to be applied for air tightness (orange) . . . 29
4.4 Locations where the epoxy adhesive is applied to the spar and bellows using q-tips . . . 29
4.5 Actuator attached to the test stand and connected to the tubes and wiring . . . 30
4.6 Failure of the inner sheet due to bearing forces . . . 33

5.1 Rendering of the test object with the bellows in red, spars in grey, trailing edge in yellow and inner sheet in black . . . 35
5.2 Deflection tests with Up (U), Neutral (N) and Down (D) positions . . . 36
5.3 Deflection speed test 1a, manually sampled with the first deflection peak and the change in input as sample points . . . 36
5.4 Deflection speed test 1b, manually sampled with the first deflection peak and the change in input as sample points . . . 37
5.5 Angular velocity for the deflection speed test coming from Figures 5.3 and 5.4 . . . 37
5.6 Test model and corresponding structural model . . . 38
5.7 Stiffness test deflections versus weight for all load cases and both tests (test 1b = T1 & test 2 = T2) 39
5.8 Deformation of the bottom part of the trailing edge with the 500 g weight attached . . . 40
5.9 Stiffness test hysteresis versus weight for all load cases . . . 40
5.10 Equivalent torsional stiffness coefficients for both stiffness tests and all weights included . . . 41
5.11 Equivalent torsional stiffness coefficients for both stiffness tests with weight ranging from 100-500g . . . 41
5.12 Damping test deflection versus time response for deflated (vacuum) neutral and inflated (10 psi) cases . . . 42
5.13 Damping test angular velocity versus time response for deflated (vacuum) neutral and inflated (10 psi) cases . . . 42
5.14 Damping coefficients determined from the damping tests, T1 and T2 are neutral, T3 is deflated (vacuum) and T4-T6 are inflated (10 psi) . . . 43
5.15 Absolute peak angular velocity versus damping coefficient for the damping tests, where neutral is atmospheric pressure, deflated is vacuum and inflated the pressure difference equals 10 psi . 44

6.1 Validation of the coefficients, as given in Table 6.1, for the torsional spring damper system from Equation (6.1) where the dotted line represents the model and the solid lines are the test results 46
6.2 Final angle for a single bellow with different parameters and the corresponding shapes for $\frac{b_{\text{bot}}}{b_{\text{top}}} = 1$ and $\frac{b_{\text{bot}}}{b_{\text{top}}} = 1.5$ . . . 48
6.3 Final angle for a single bellow with different parameters and the corresponding shapes for $\frac{b_{\text{bot}}}{b_{\text{top}}} = 2$ and $\frac{b_{\text{bot}}}{b_{\text{top}}} = 4$ . . . 48

LIST OF TABLES

1.1 LE thickness distribution 5
1.2 TE thickness distribution 5

2.1 Analyzed flight conditions with the different inputs for AAA and XFOIL 9
2.2 Calculated load on the morphing part of the wing, morphing part neutral for the flight conditions given in Table 2.1 and the stall analysis from Figure 2.4 10
2.3 Calculated moment on the morphing part of the wing, morphing part neutral for the flight conditions given in Table 2.1 and the stall analysis from Figure 2.4 11
2.4 Calculated load on the morphing part of the wing, morphing part deflected +15 degrees 12
2.5 Calculated moment on the morphing part of the wing, morphing part deflected +15 degrees . . 12
2.6 Calculated load on the morphing part of the wing, morphing part deflected -15 degrees 13
2.7 Calculated moment on the morphing part of the wing, morphing part deflected -15 degrees . . 13
2.8 Summary of the minimum and maximum loads expected on the morphing part of the flap, which are found in the descent flight configuration 16
2.9 Ratio of maximum to (absolute) minimum forces and moments and load factor ratio 16

4.1 Material properties of polycarbonate [33] 25
4.2 Material properties of typical aircraft aluminum grades [33] 26
4.3 Material properties of Kevlar® and graphite [33] 26
4.4 Bill of material for the assembly of a single actuator 28
4.5 Cross section dimensions for the aluminum bars and connectors used in the test stand 30
4.6 Weight estimation of the parts and flap 31

5.1 Deflections (Δd) and deflection angles (δ_{morph}) for the deflection tests 36
5.2 Deflections stiffness test 1b in mm where 1 represents the initial state, 2 the deflected state with weight attached and 3 the hysteresis. Neutral (N) is no pressure supplied and for Inflated (I) 10 psi (0.69 bar) is supplied to the bellows 38
5.3 Deflections stiffness test 2 in mm where 1 represents the initial state, 2 the deflected state with weight attached and 3 the hysteresis. Neutral (N) is no pressure supplied and for Inflated (I) 10 psi (0.69 bar) is supplied to the bellows 39
5.4 Equivalent torsional stiffness for both stiffness tests in $[\mathrm{N \cdot m/rad}]$ 41
5.5 Natural frequency and torsional stiffness constant calculated from the dynamic tests, where κ is the torsional stiffness calculated with the mass moment of inertia from CATIA™ and κ_2 is calculated with the mass moment of inertia from CATIA™ + 18.7% 44

6.1 Empirically determined constants and coefficients for the torsional spring damper system as given in Equation (6.1), where κ is the torsional stiffness calculated with the mass moment of inertia from CATIA™ and κ_2 is calculated with the mass moment of inertia from CATIA™ + 18.7% 45

NOMENCLATURE

Latin

a = Ellipse horizontal radius [mm]
b = Ellipse vertical radius [mm]
c = Chord [m]
c_l = Sectional lift coefficient [−]
d = Deflection [deg]
d_1 = First deflection peak [mm]
d_2 = Second deflection peak [mm]
F = Force [N]
f = Frequency [Hz]
h = Altitude [m]
I = Mass moment of inertia [$\mathrm{g \cdot m^2}$]
M = Moment [$\mathrm{N \cdot m}$]
M = Mach number [-]
N = Super-ellipse power factor [m]
n = Load factor [−]
p = Pressure [bar]
Re = Reynolds number [−]
(t/c) = Thickness over chord ratio [−]
V = Velocity [m/s]
W = Weight [N]
(x/c) = Chordwise location ratio [−]

Greek

γ = Flightpath angle [deg]
Δ = Difference [−]
δ = Natural logarithm of ratio of two successive deflections [−]
δ = Deflection [deg]
δ = Partial [−]
ζ = Damping ratio [−]
θ = Deflection angle [rad]
$\dot{\theta}$ = Deflection speed [rad/s]
$\ddot{\theta}$ = Deflection acceleration [$\mathrm{rad/s^2}$]
κ = Equivalent torsional spring stiffness [$\mathrm{N \cdot m/rad}$]
λ = Ellipse factor for circumference calculation [−]
τ = Torque [$\mathrm{N \cdot m}$]

Subsctripts

a = Atmosphere
bot = Bottom height of the super-ellipse
bot = Bottom part of the actuator
current = Current (time wise) situation
dynamic = Dynamic test
i = Inboard
f = Flap
morph = Morping part of the wing
n = Natural
o = Outboard
pivot = Pivot (rotation) point of the actuator
static = Static test
top = Top height of the super-ellipse
top = Top part of the actuator

1

INTRODUCTION

Ever since the transition to metal in airframes and aerostructures, most wings have been stiff and rigid. The concept of variable stiffness has not been applied in aviation. The concept of High-Lift Devices (HLDs), ailerons and other movables have developed over the years. The understanding of the physical phenomena has increased significantly. In 1975, Smith [1] described the five main effects of multi-element airfoils, which proved the functionality of high lift devices. Since then, the knowledge about HLD has increased further, however optimization of HLDs is still subject to difficulties. Besides that, the High Lift Devices which are currently implemented are all simple, rigid systems, consisting of a single leading element and a single trailing element [2]. This means that HLDs and the other movables are discrete systems with a constant stiffness.

Since the aircraft efficiency is pushed to new limits, new technologies have to be applied to make aircraft operate more fuel efficient. Continuous camber variation is one of these new technologies. HLDs are used to overcome the conflicting requirements between cruise and take-off and landing. However, if the climb and cruise segment are considered in more details, there is an optimization possible for more segments in flight. Since fuel is being burned, the lift coefficient is not constant during climb and cruise. The optimum airfoil shape with the optimum Lift over Drag ratio is varying over the complete mission. Variable camber is suitable to fill this gap. The introduction will continue with background information on variable camber and variable stiffness in Section 1.1. For the purpose of this thesis a Cessna Citation X inboard flap has been obtained, therefor more information on the Cessna Citation X and the inboard flap is given in Section 1.2. The chapter will then conclude with the research questions and aims in Section 1.3.

The proceeding chapters will give more detailed information of this study. The loads, which are experienced on the Cessna Citation X flap, are estimated in Chapter 2. Chapter 3 shows the preliminary design of the actuator and the test setup. The production of the final design is described in Chapter 4. The results of the structural testing are given in Chapter 5. The test data is used to build analytic models, which can be applied to this actuator. These models are given in Chapter 6. The report finishes with the conclusions and recommendations in Chapter 7.

1.1. BACKGROUND INFORMATION ON VARIABLE CAMBER AND VARIABLE STIFFNESS

Variable camber research is seen in several concepts. Examples of these projects are the F-111 Mission Adaptive Wing [3, 4], Project NEW [4], NASA's Lockheed L-1011 [5], Grumman TERFENOL-D [6, 7], FishBAC [8–10] and Project SADE and ADIF [11, 12]. These projects use rotary actuators, magnetostrictive materials, finger and belt rib concept and a fishbone structure for actuation.

The FishBone Active Camber (FishBAC) morphing system is interesting for this project. The structure they use for variable camber is shown in Figure 1.1. The leading 35% of the chord is the load carrying D-spar. The trailing 15% of the chord is solid, where the structure for active camber is applied in between. As the name suggests, the structure resembles the structure of a fishbone. The bending beam has a thickness of 1.5 mm and 14 stringers are connected to it, which attach to the composite skin. The thickness of the stringers is 0.75 mm and do not add to the spine stiffness in morphing direction. The morphing in the prototype is induced by a pulley, which can pull the trailing edge up and down. The total up and down deflection equals 40mm at the trailing edge, which is 13.3% of the total airfoil chord.

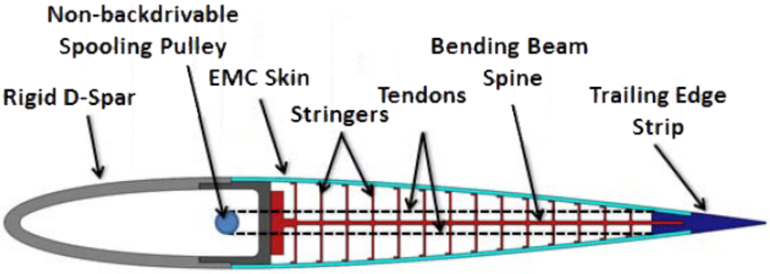

Figure 1.1: FishBAC structure [8]

Other research is done in Shape Memory Alloy (SMA) [13–17] and Piezoelectric actuators (PZT) [18–20]. SMA are actuated by the application of heat, but also actively cooled SMA and ferromagnetic SMA exist, which was investigated by Wang et al. [13]. The concept of Sofla et al. [14] was capable of inducing 4.31 degrees of rotation. This was achieved by a single Antagonistic Flexural unit Cell (AFC) as shown in Figure 1.2. The pivot point is located in the center of a cell, which consists of two actuators. Applying heat to one side of the actuator extends the actuator on that side, whereas the implied load contracts the other actuator. A beam made up by 84 linked AFCs could bend from flat plate to full circle. The AFCs are able to sustain in this shape without the use of any external power.

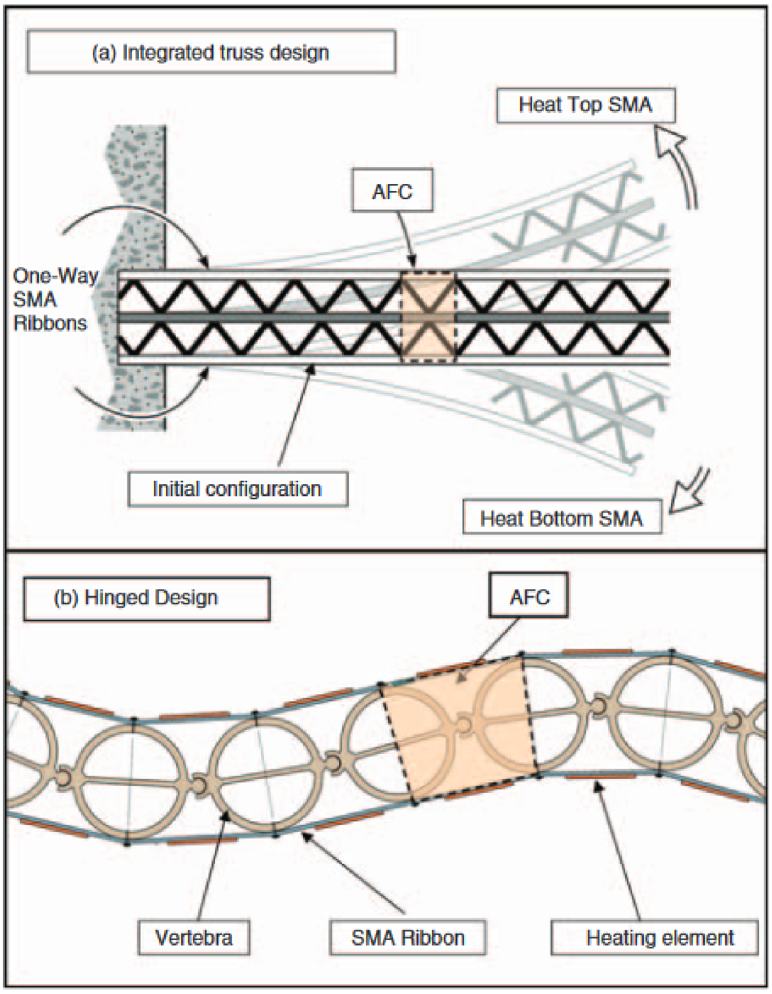

Figure 1.2: AFC structure for an integrated truss design and a hinged design [14]

Piezoelectric actuation is induced by, for example, two wafers with opposite poling, resulting in a bending moment. The concept of Heinze and Karpel [19] was a piezoelectric tab, for which the tab deflection was less than 3 degrees. Vos et al. [20] used post-buckled precompressed (PBP) piezoelectric bender actuators and were able to reach deflections up to 15.25 degrees. This concept is shown in Figure 1.3, where it can be seen that the structure consists of a D-spar as well. Attached to the D-spar are the PBP actuators, which extended to 98% chord of the trailing edge. The skin was made from latex, whereas the D-spar was made from carbon epoxy. Applying an electric field to the actuators made them deflect up and down. The concept was applied to the aileron of a UAV, for which it is shown that the roll control increased by 38% compared to conventional ailerons.

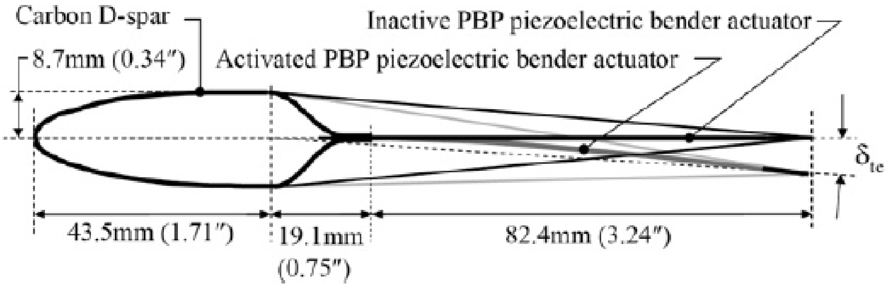

Figure 1.3: Variable camber by PBP piezolectric actuation [20]

Another method to induce variable camber is the Pressure Adaptive Honeycomb (PAH) structure. The benefit of the pressure adaptive honeycomb, as proposed by Vos et al., is that it can be applied to primary structures. Several other concepts are made of materials which are not in the FAR23/25 and 27/29 database. The pressure adaptive structure is made of the materials from the database. Other benefits are the high mass-specific energy density and energy efficiency. By applying a pressure differential of 40 kPa, the camber can be changed up to 5% [21–26]. The PAH concept can be seen in Figure 1.4, where the honeycomb structure is clearly visible at the trailing 35% of the chord. The honeycomb is built in such a way that in the relaxed state, when no pressure is applied, the maximum curvature is achieved. Inflating the honeycomb cells straightens the structure and decreases the amount of camber.

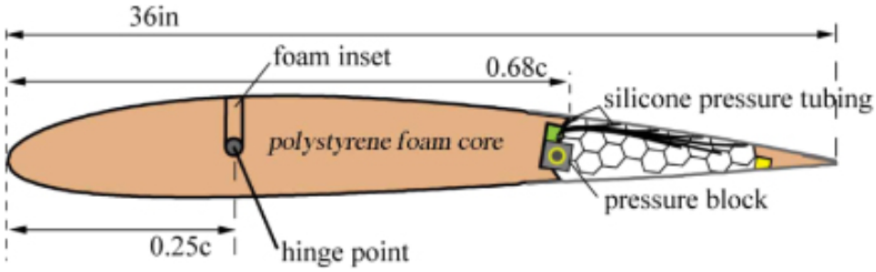

Figure 1.4: Pressure adaptive honeycomb topology [26]

Variable camber can optimize the lift coefficient, but the wing lift gradient can be adjusted as well. Adjusting the wing lift gradient will decrease the gust upsets, since the response will be smaller, in other words they alleviate the gust loading. Examples in modern aircraft where gust load alleviation is applied are the Airbus A380, Airbus A350 and the Boeing 787 [27]. Adjusting the wing lift gradient will not particularly increase the efficiency of the aircraft, but will contribute to smoother rides, less fatigue damage and improved aviation safety in case of microbursts [28]. Barrett and Barrett [28] proved that a variable stiffness trailing edge will change the lift coefficient gradient of the aircraft which is seen in Figure 1.5. Barrett and Barrett used the concept of Vos in a slightly different way, as can be seen in Figure 1.6. The PAH is applied symmetrically on two sides of a flexible substrate and are bounded by end blocks. Applying different pressures to the upper and lower side will induce the deflection, whereas increasing the pressure in the upper and lower region simultaneous can be used to change stiffness. A Balanced Cell Differential Pressure of 50 kPa makes the deformations due to the stiffness so small that the airfoil behaves as if it was rigid. Due to the free floating 15% chord of the trailing edge and a lower BCDP the lift coefficient gradient is reduced.

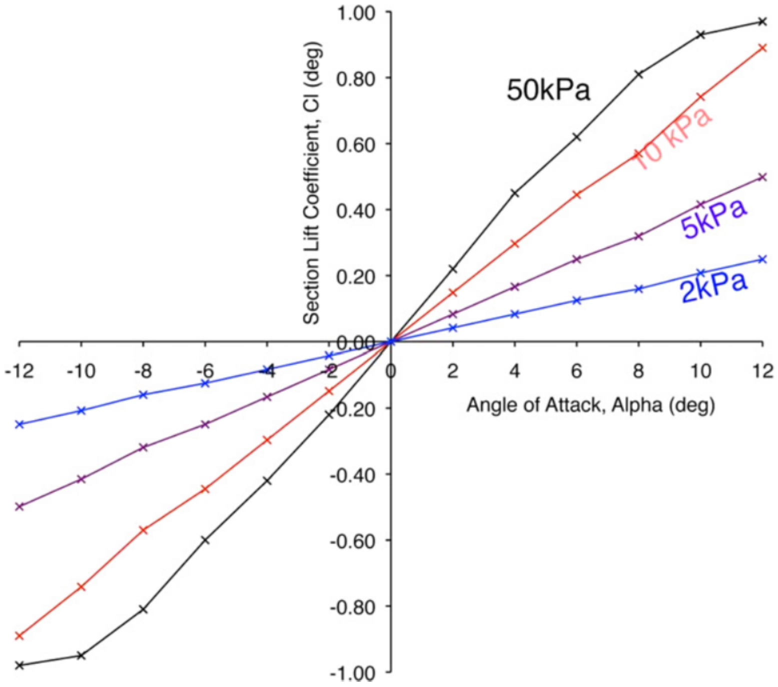

Figure 1.5: Lift curves for a wind tunnel model in null position at a variety of BCDP [28]

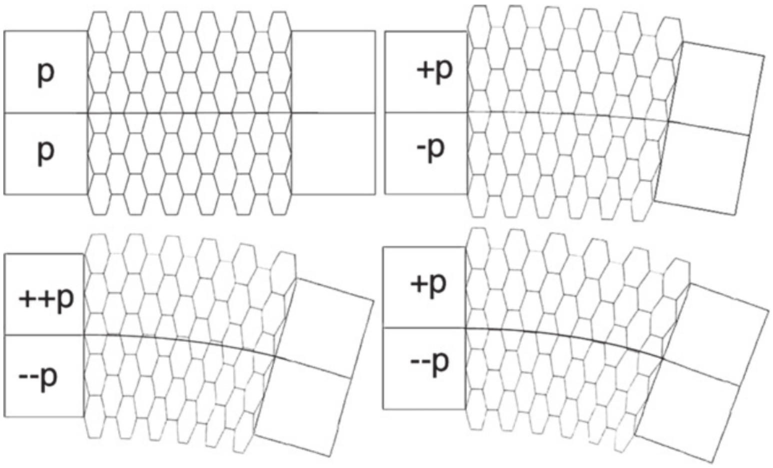

Figure 1.6: Bidirectional actuation scheme of PAH actuator [28]

1.2. THE CESSNA CITATION X INBOARD FLAP

The Cessna Citation X saw its maiden flight at the end of 1993 and it became available on the market in 1996 [29]. It's a twin engine business jet capable of flying Mach 0.92 with a maximum range of 5685 km. The wing spans 19.48 m without the winglets, which are optional to install on older versions and became the standard on new deliveries. The wing aspect ratio is 7.8, with a mean aerodynamic chord of 2.50 m and a quarter chord sweep of 37 degrees. The dihedral angle of the wing measures 2 degrees. For take-off and landing the wing has three fowler type single slotted flaps, for which the actuation system can be found in the Cessna Citation Excel cutout in Figure 1.7. This wing gives a close approximation of the Cessna Citation X wing. The differences between the Excel wing and the X wing are the sweepback (37 degrees quarterchord for the X versus 0 degrees at 35% of the chord for the Excel) and the number of fowler flaps (three for the X versus two for the Excel). In the cutout in Figure 1.7, the flaps are given with C7, the titanium flap tracks with C8 and C9, where C10 gives the flap actuation linkage.

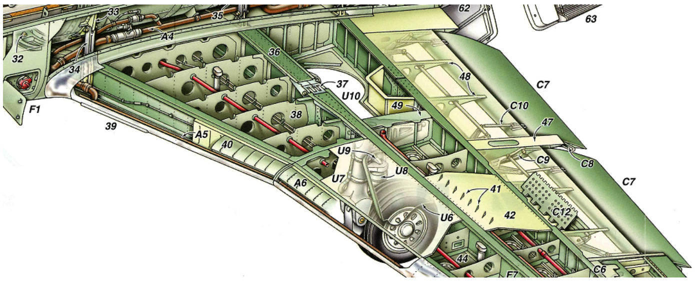

Figure 1.7: Cutaway of the Cessna Citation Excel wing [30]

For the test setup, the dimensions of the Cessna Citation X inboard flap are measured. The inboard flap of the Cessna Citation X measures 1670 mm in spanwise direction and 705 mm in chordwise direction. From the flap, the inboard and outboard thickness distributions can be measured. The normalized distribution is found in Table 1.1 for the Leading Edge (LE) and in Table 1.2 for the Trailing Edge (TE). Since it was not possible to measure the thickness in the middle of the flap, it is assumed that the thickness distribution is varied linearly over the span.

Table 1.1: LE thickness distribution

(x/c_f) [-]	$(t/c_\mathrm{f})_\mathrm{i}$ [-]	$(t/c_\mathrm{f})_\mathrm{o}$ [-]
0.00	0.000	0.000
0.05	0.110	0.083
0.10	0.124	0.094
0.15	0.126	0.100
0.20	0.126	0.100
0.25	0.122	0.097
0.30	0.121	0.095
0.35	0.114	0.088
0.40	0.105	0.082
0.45	0.098	0.079
0.50	0.091	0.074

Table 1.2: TE thickness distribution

(x/c_f) [-]	$(t/c_\mathrm{f})_\mathrm{i}$ [-]	$(t/c_\mathrm{f})_\mathrm{o}$ [-]
0.50	0.091	0.074
0.55	0.082	0.068
0.60	0.071	0.063
0.65	0.065	0.054
0.70	0.056	0.047
0.75	0.047	0.040
0.80	0.040	0.034
0.85	0.033	0.029
0.90	0.025	0.024
0.95	0.019	0.018
1.00	0.015	0.013

Since the flap is not symmetric, camber has been added to the airfoil profile until it resembles the camber of the flap. It was found that 3% camber and the location of maximum camber at 40% gave a nice fit to the real flap geometry. The thickness distributions and the addition of camber is found in Figure 1.8. Note that this addition of camber does not change the thickness distribution, although it does change the angle of 0 degrees deflection for the trailing edge. In Figure 1.8 also a center airfoil profile is being shown. This is assumed to be a linear interpolation of the inner and the outer airfoils.

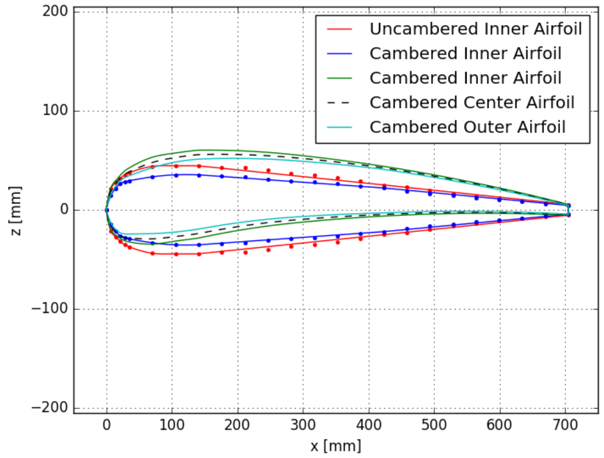

Figure 1.8: Measured thickness distributions and cambered profiles for Cessna Citation X inboard flap

The inboard flap is located in the wing root section. The wing root section shows some positive dihedral, which is also visible in the flap. Since it is easier to apply an adaptive structure to a straight line, it is desired to find the chordwise location with the least amount of dihedral as possible. The trailing edge shows less dihedral compared to the leading edge. The line which satisfies the dihedral requirement and which still has 'enough' absolute thickness is located near 30% of the trailing edge. From Table 1.2 it is found that the inboard, normalized thickness at this location is 0.056, where the outboard equals 0.047.

1.3. RESEARCH QUESTIONS AND AIMS

The research is focused on demonstrating practical applications for morphing structures and determining the structural behavior of the pressure adaptive trailing edge. The main research and sub research questions are formulated as:

> *What implications are present for manufacturing a full scale business jet inboard flap by designing and manufacturing the flap?*

1. What is the adaptation of the structure to apply wing morphing?
2. What is the net effect on the flap weight system?
3. How to deal with the "closeout problem"[1]?
4. How to translate the 2D model to a 3D wing?
5. What is the optimal wedge geometry to provide enough stiffness for up and downward deflection?

> *What is the structural behavior of a Pressure Adaptive inboard flap trailing edge on a business jet aircraft by performing bench testing on a full scale flap?*

1. What is the relation of stiffness and damping with pressure of the pressure adaptive structure?
2. Is the Pressure Adaptive Bellow structure stiff enough to withstand the design loads of the flap?
3. What are the deflections and deflection speeds which can be reached by the actuator?

The main objective of this study is demonstrating the functionality of the pressure adaptive trailing edge applied to a full scale business jet wing. This is done by performing bench tests of the actuator system, to measure the deflection angles and stiffness of the pressure adaptive bellows. The faculty of aerospace engineering at The University of Kansas obtained a Cessna Citation X inboard flap which will be used for this purpose. The goal of this project will be providing a variable stiffness and variable camber trailing edge to the design of this flap.

---

[1] The closeout problem refers to the air tightness of the pressure adaptive structure

2

LIFT COEFFICIENT ANALYSIS AND LOAD ESTIMATION

This chapter will estimate the loads on the morphing part of the flap. For this estimation, the aircraft has to be modeled, which is described in Section 2.1. In the following sections the loads are estimated, Section 2.2 has the results for the morphing part in neutral position, for Section 2.3 and Section 2.4 the morphing part of the wing is deflected down and up respectively. The load changes with morphing is shown in Section 2.5. Section 2.6 makes an estimate for the gust and maneuvering loads by means of a V-n diagram. In Section 2.7, this chapter is wrapped up with an estimation of the loading on the morphing part of the flap.

2.1. AIRCRAFT MODEL AND LIFT COEFFICIENT ANALYSIS

For the analysis of the lift coefficient, different loading situations of the Cessna Citation X are considered. The Cessna Citation X is modeled in DARcorporation's Advanced Aircraft Analysis (AAA) software to find the sectional lift coefficient, using the trim function. This lift coefficient is used in a 2D analysis of the local airfoil in XFOIL. XFOIL produces the local pressure distributions over the airfoil. With the pressure distributions, the loads on the trailing part of the flap can be estimated.

The AAA model uses the dimensions from Jane's All the World's Aircraft [29] and the model is compared to the airplane three view in Figure 2.1. The red line represents the AAA model and it can be seen that the model is a quite accurate representation of the actual aircraft. However, still some assumptions had to be made. According to the "Incomplete Airfoil Guide" [31] by David Lednicer, the Cessna Citation X uses the Cessna 7500 airfoil and the Cessna 7504 airfoil for the root and tip respectively. The shapes of these airfoils could not be found, therefor it is chosen to work with a modestly thick supercritical airfoil: the MS(1)-0313 from NASA. Other estimations had to be made for the Center of Gravity (CG), where AAA aided in providing CG locations for some airplane components. The center of gravity estimation is then checked on stability, take off rotation and trimmability. AAA suggests the most forward and afterward CG locations vary with 10-21% for business jet aircraft, which is used to estimate the forward and afterward CG locations for the Cessna Citation X.

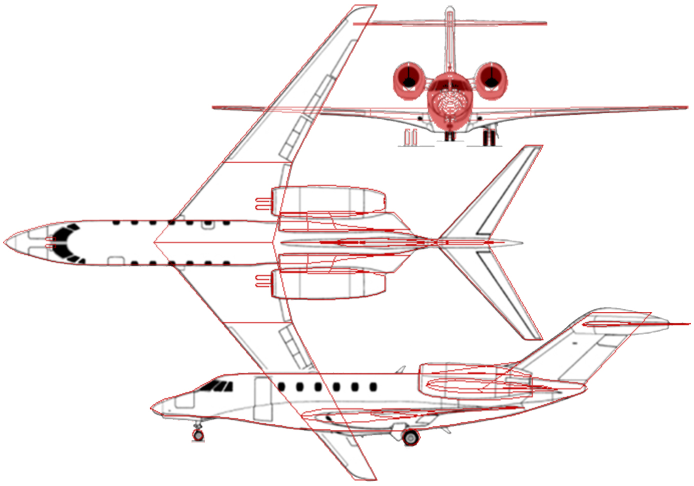

Figure 2.1: Airplane three view from Jane's All the World's Aircraft [29] compared to the AAA model (Red)

The typical flight segments have been analyzed and split up in 6 parts, with corresponding sectional lift coefficient and flap angles. The wing lift distributions for the 6 flight conditions can be found in Figure 2.2. The flap is located between 11.8% and 33.2%. Since it can be seen that the lift distribution is fairly linear around this point, it is chosen to take the sectional lift coefficient to be the average lift coefficient on the section. The analyzed Flight Conditions (FC) and settings can be found in Table 2.1. For all flight conditions the aircraft was trimmable, however for the descent configuration the aircraft did not trim in thrust and drag direction. This was caused by the negative flight path angle and the drag being so small that negative thrust would have been necessary to compensate for the tilted weight force. It was therefor chosen to have the spoilers extended for this flight condition, where it is retracted for the other conditions.

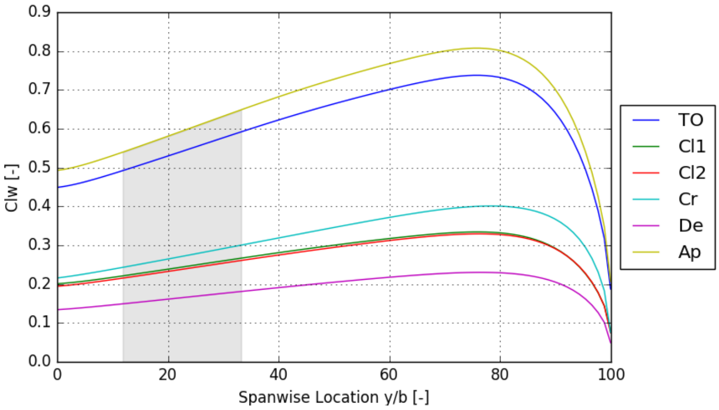

Figure 2.2: Spanwise lift distribution for different flight conditions for the Cessna Citation X from AAA with the inboard flap location highlighted

The Mach numbers are the numbers used for the analysis in XFOIL and correspond to the altitude and flight speed. The only changes are in cruise and descent configuration, where the analysis is performed on a lower Mach number. This is because on higher Mach numbers, XFOIL has difficulties to converge. It is expected that the pressure distribution is still a good estimation for the preliminary load calculations.

Table 2.1: Analyzed flight conditions with the different inputs for AAA and XFOIL

FC	h	V	c_l	δ_f	γ	W_current	$Re \cdot 10^6$	M	Spoiler Setting
	[km]	[km/h]	[deg]	[deg]	[deg]	[kN]	[−]	[−]	[−]
Take-Off	0	300	0.542	5	0	160.5	20.7	0.245	Retracted
Climb 1	1.2	500	0.244	0	18	158.5	30.0	0.414	Retracted
Climb 2	5.9	648	0.238	0	15	156.5	26.1	0.568	Retracted
Cruise	12	850	0.271	0	0	149.5	18.0	0.600	Retracted
Descent	6	750	0.165	0	-12.5	142.0	29.9	0.600	Deployed
Approach	0.5	240	0.594	30	-3	141.5	16.8	0.197	Retracted

Since the flaps are fowler type flaps, the reference chord length varies when the flaps get deployed. The reference chord length taken for the retracted flight conditions is determined in AAA and equal 3.47 m at 22.5% span location, which is exactly the middle of the flap. Since the flap is partly covered in retracted condition, the covered versus uncovered length had to be found. In the airplane 3-View in Figure 2.1 the inboard flap is presented in retracted condition. When this is measured, it is found that the uncovered average flap chord length in retracted state equals 0.345 m. Since the full flap measures 0.705m in chordwise direction, the flap can extend the chord by 0.360 m. For the full deflection in the approach configuration this full extension is reached, making the reference chord length 3.83 m. For the take-off configuration it is assumed that the flap partially extends and deflects. In this condition it is chosen to have a flap extension of 0.160 m, making the reference chord length 3.63 m.

It should be noted that the pressure distribution is calculated in XFOIL with viscous effects. XFOIL uses the wake trajectory of the inviscid solution for that specific angle of attack. This assumption is made to decrease the calculation time significantly. The effect of this assumption is largest for near stall and past stall conditions, when separation is present. Separation is found in the analysis where the recovering pressure gradient is almost horizontal. It is assumed that the XFOIL predictions are sufficient for the purpose of the load estimation.

2.2. NEUTRAL MORPHING LOAD ESTIMATION

For the flight conditions in Table 2.1, the pressure distributions are given in Figures 2.3a and 2.3b. It can be seen that flap deflections increases the pressure difference on the morphing part of the wing, which is highlighted. The flap deflection, however, decreases the reference chord length in XFOIL. Since XFOIL does not take fowler type of flap motions, a plain flap configuration is taken for the estimation. The reference chord compensates for this deficit.

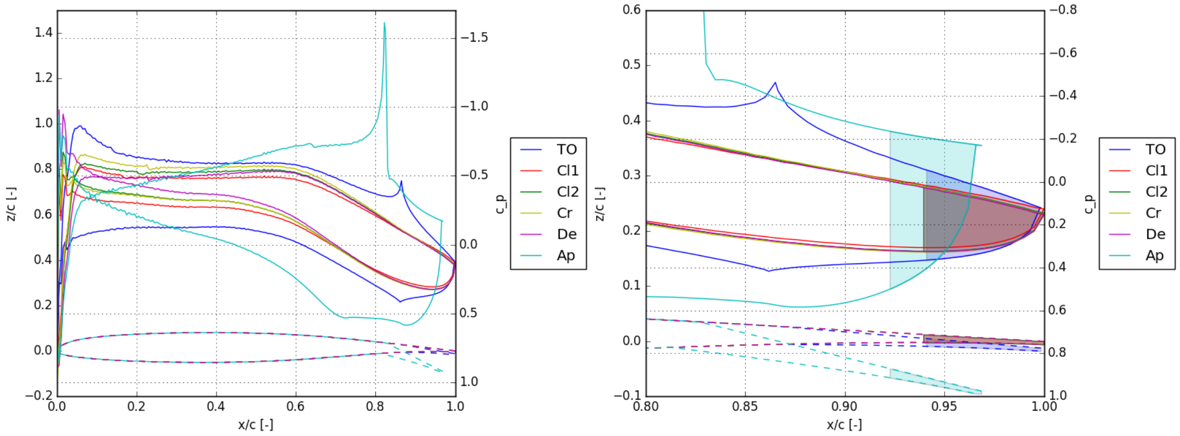

(a) $0.0 \leq x/c \leq 1.0$

(b) $0.8 \leq x/c \leq 1.0$

Figure 2.3: Pressure distributions for different flight conditions, morphing part neutral as analyzed in XFOIL with the flight conditions as given in Table 2.1

The stall conditions are analyzed for different angles of attack as well. After the wing has stalled the pressure distribution over the section still changes. This can be seen in Figures 2.4a and 2.4b. The estimation of the loading is seen in Table 2.2. For the stall speed the loading is determined with a speed of approximately 140kts, which is assumed to be the stall speed in clean configuration. The loading is found to be the highest in the descent configuration, because the loading percentage ($\frac{\delta c_l}{c_l}$) is the highest. The lowest forces are actually seen with flap deflections, since the fraction gets smaller. The flap deflection not only changes the pressure of the deflected part, but interferes with the complete pressure distribution.

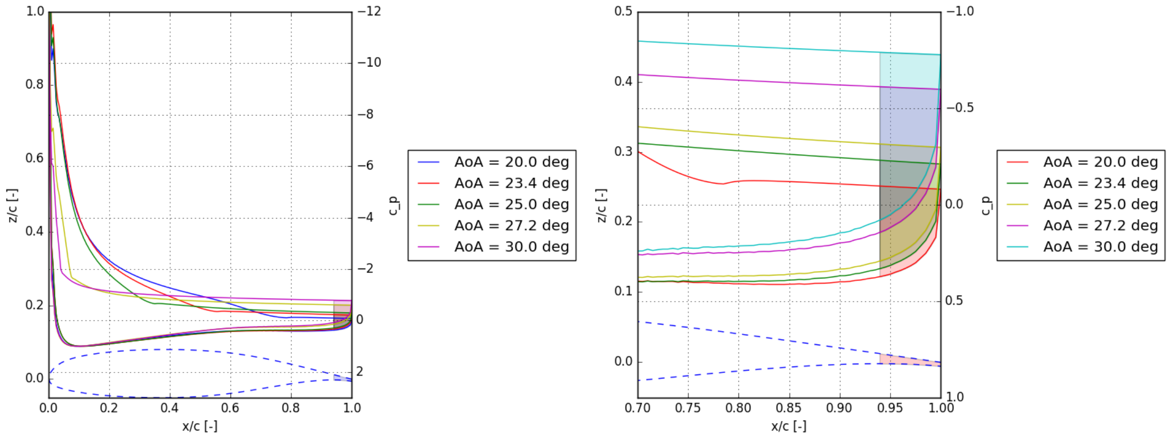

(a) $0.0 \leq x/c \leq 1.0$

(b) $0.7 \leq x/c \leq 1.0$

Figure 2.4: Pressure distributions stalled MS(1)-0313 airfoil, analyzed in XFOIL with $Re = 29.9 \cdot 10^6$

Table 2.2: Calculated load on the morphing part of the wing, morphing part neutral for the flight conditions given in Table 2.1 and the stall analysis from Figure 2.4

FC	α [deg]	F_{morph} [N]	c_l [−]	δc_l [−]	$\frac{\delta c_l}{c_l}$ [%]
TO	-1.03	83.3	0.54	0.0162	2.98
Cl1	-1.41	153.7	0.24	0.0126	5.17
Cl2	-1.61	161.2	0.24	0.0129	5.40
Cr	-1.42	129.5	0.27	0.0128	4.73
De	-2.11	209.7	0.16	0.0126	7.64
Ap	-7.78	79.7	0.62	0.0240	3.88
St1	20.00	84.2	2.10	0.0227	1.08
St2	23.40	100.2	2.02	0.0271	1.34
St3	25.00	108.4	1.86	0.0293	1.57
St4	26.00	119.6	1.66	0.0323	1.95
St5	27.20	135.3	1.52	0.0365	2.40
St6	28.40	144.9	1.51	0.0391	2.59
St7	29.60	153.0	1.53	0.0413	2.71
St8	30.00	155.8	1.53	0.0421	2.75

The trailing 30% of the pressure distribution multiplied with the moment arm is integrated, which results in the bending moment. As the morphing part is rotating around a pivot point, the bending moment is important to determine the rotational behavior at the morphing hinge. It is assumed that the pivot point is located at the 70% chord line and the trailing edge has a free floating end. This means that the forces of the leading part of the wing at that location do not influence the bending moment. The bending moment can be found in Table 2.3, where the reference arm, noted with d_{pivot}, can be found as well. This arm would have to be applied if the force was a point force instead of a distributed force. It represents the centroid of the distributed lift force on the morphing part of the flap. The last column shows the percentage of the morphing part of the flap where this reference force has to be applied. This equals around 37.5% in the stalled condition, around 35% for the conditions with retracted flaps and moves forward to 32.3% and 25.6% with deployed flaps for take-off and approach conditions respectively. The highest moment is found in descent flight condition and equals 15.24 $N \cdot m$.

Table 2.3: Calculated moment on the morphing part of the wing, morphing part neutral for the flight conditions given in Table 2.1 and the stall analysis from Figure 2.4

FC	M_{pivot} [N·m]	d_{pivot} [mm]	$\frac{d_{\text{pivot}}}{c_{\text{morph}}}$ [%]
TO	5.65	67.8	32.3
Cl1	11.29	73.4	35.0
Cl2	11.74	72.9	34.7
Cr	9.39	72.5	34.5
De	15.24	72.7	34.6
Ap	4.28	53.7	25.6
St1	6.62	78.6	37.4
St2	7.87	78.6	37.4
St3	8.52	78.6	37.4
St4	9.41	78.7	37.5
St5	10.65	78.8	37.5
St6	11.41	78.8	37.5
St7	12.05	78.8	37.5
St8	12.27	78.8	37.5

2.3. POSITIVE MORPHING LOAD ESTIMATION

Since the actuator is able to move the trailing part up and down, the forces will also change on the morphing part of the flap and the moment will change on the pivot point. The same flight conditions as in Section 2.1 are used for this analysis with the same section lift coefficients. The trailing 30% of the flap is the morphing part, which for this analysis is handled as a discrete, plain flap. The deflection is 15 degrees in positive direction, which is downwards in aircraft conventions. The pressure distributions on the airfoil can be found in Figure 2.5. Here it is seen that the loading of the airfoil shifted more to the trailing edge. Because of the discrete plain flap, a clear peak in the pressure distribution can be found around the morphing hinge, except for the approach configuration. Looking at the pressure distribution for this configuration, it is likely that separation is found at the trailing edge. This is caused by the plain flap assumption, where it actually is a fowler type of flap. Another noticeable difference is the sharpness of the loading near the end. The recovering pressure gradient on the top surface is significant.

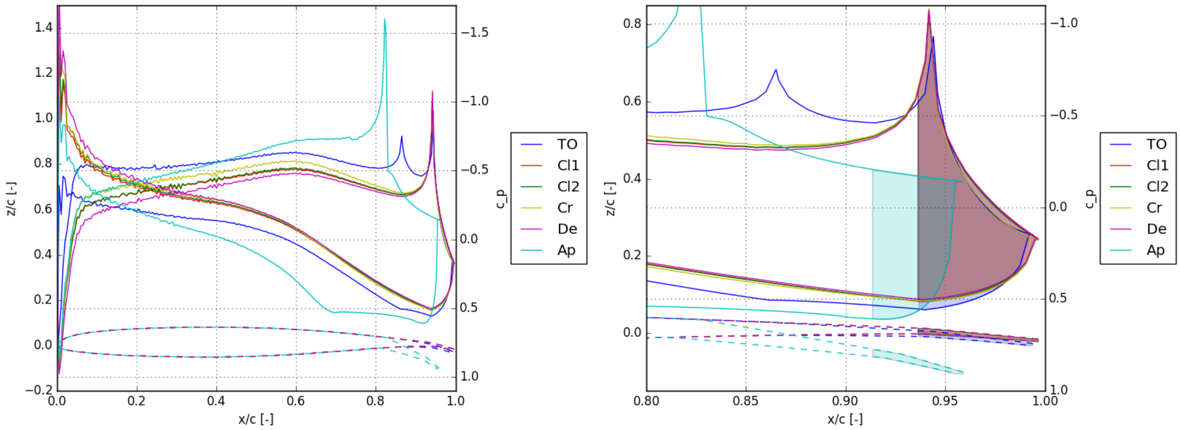

(a) $0.0 \le x/c \le 1.0$

(b) $0.8 \le x/c \le 1.0$

Figure 2.5: Pressure distributions for different flight conditions, morphing part deflected +15 degrees analyzed in XFOIL with the flight conditions given in Table 2.1

Similar as for the neutral case, the forces have been calculated, which can be seen in Table 2.4. Except that the Mach numbers had to be lowered a bit more for convergence, for which the new Mach numbers are given. This might change the pressure distributions slightly, but as before it should still be sufficient to calculate the loads in a preliminary phase. The highest forces are found in the descent configuration, where the force tripled. The approach condition shows the least increase compared to the neutral case, but is the lowest. All other forces tripled except take-off, where it doubled compared to the neutral position.

Table 2.4: Calculated load on the morphing part of the wing, morphing part deflected +15 degrees

FC	α [deg]	M [−]	F_{morph} [N]	c_l [−]	δc_l [−]	$\frac{\delta c_l}{c_l}$ [%]
TO	-4.25	0.245	189.2	0.54	0.0367	6.74
Cl1	-5.04	0.314	470.1	0.25	0.0386	15.43
Cl2	-5.04	0.368	479.3	0.24	0.0383	15.64
Cr	-4.66	0.500	372.1	0.28	0.0369	13.38
De	-5.64	0.300	631.6	0.17	0.0381	22.06
Ap	-8.31	0.197	98.4	0.63	0.0297	4.75

Since the pressure differences mainly increased near the pivot, it is expected that the moment does not increase as much compared to the forces. The results of the moment calculations can be seen in Table 2.5. For the takeoff condition the moment doubled, climb, cruise and descend are 2-2.5 times higher compared to the neutral case, whereas the approach condition shows the least increment.

Table 2.5: Calculated moment on the morphing part of the wing, morphing part deflected +15 degrees

FC	M_{pivot} [N·m]	d_{pivot} [mm]	$\frac{d_{\text{pivot}}}{c_{\text{morph}}}$ [%]
TO	10.54	55.7	26.5
Cl1	27.80	59.1	28.2
Cl2	28.13	58.7	27.9
Cr	21.26	57.1	27.2
De	37.19	58.9	28.0
Ap	5.40	54.9	26.1

2.4. NEGATIVE MORPHING LOAD ESTIMATION

Since it is expected that the morphing part of the flap is able to decamber the airfoil, a negative morphing can be achieved. This negative morphing will be similar to the positive morphing, but then deflected upwards with 15 degrees. Looking at the pressure distribution in Figure 2.6, this means that the airfoil will be loaded more towards the leading edge. For the same flight conditions a negative loading is achieved on the rear of the airfoil, except for the approach configuration.

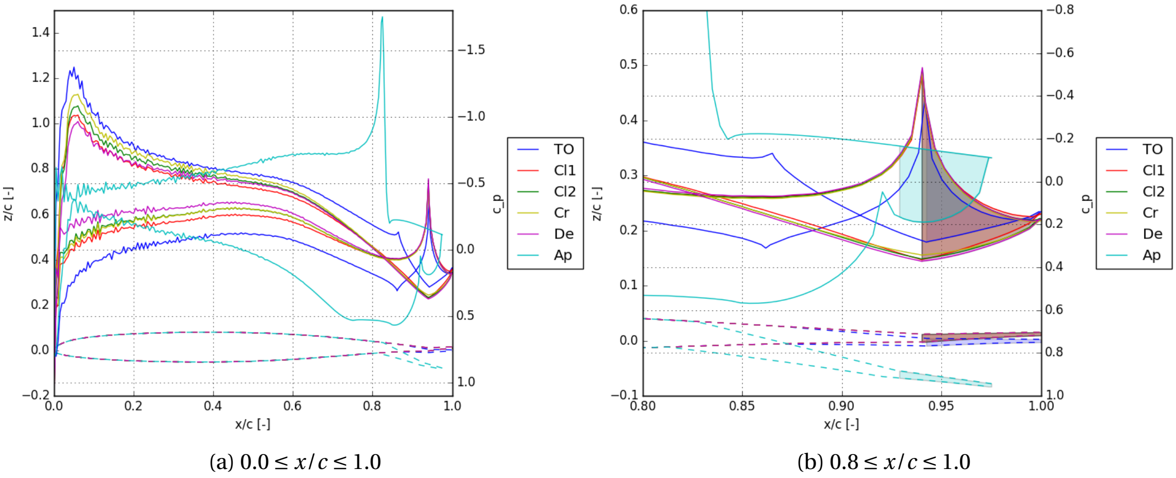

(a) $0.0 \leq x/c \leq 1.0$ (b) $0.8 \leq x/c \leq 1.0$

Figure 2.6: Pressure distributions for different flight conditions, morphing part deflected -15 degrees analyzed in XFOIL with the flight conditions given in Table 2.1

Since the upwards morphing of the trailing edge caused a negative loading on the trailing edge, the force will be pointing down. Therefor, all the calculated forces will be negative, except for the approach flight condition. This is seen in Table 2.6. The most negative force is seen in the descent configuration and equals 253.4 N pointing down. In approach the force will be 42.5 N pointing up.

Table 2.6: Calculated load on the morphing part of the wing, morphing part deflected -15 degrees

FC	α [deg]	F_{morph} [N]	c_l [$-$]	δc_l [$-$]	$\frac{\delta c_l}{c_l}$ [%]
TO	2.86	-36.1	0.54	-0.0070	-1.29
Cl1	2.57	-174.0	0.24	-0.0143	-5.87
Cl2	2.23	-183.4	0.24	-0.0146	-6.16
Cr	2.34	-141.0	0.27	-0.0140	-5.17
De	1.71	-253.4	0.16	-0.0153	-9.27
Ap	-6.37	42.5	0.62	0.0128	2.07

Since the forces are acting downwards, the moment changed direction as well. The moment is now acting in clockwise direction with respect to the pivot point, and equals 1.26 N·m for the take-off flight condition to 12.68 N·m for the descent configuration. In approach configuration, it still acts in counterclockwise direction and equals 2.44 N·m.

Table 2.7: Calculated moment on the morphing part of the wing, morphing part deflected -15 degrees

FC	M_{pivot} [N·m]	d_{pivot} [mm]	$\frac{d_{\text{pivot}}}{c_{\text{morph}}}$ [%]
TO	-1.26	34.9	16.6
Cl1	-8.51	48.9	23.3
Cl2	-9.06	49.4	23.5
Cr	-6.94	49.2	23.4
De	-12.68	50.1	23.8
Ap	2.44	57.3	27.3

2.5. EFFECT OF MORPHING ON LOAD ESTIMATION

It is seen that the maximum and minimum force is achieved for the descent flight condition, where the upforce is 2:49 times bigger in absolute value than the downforce. The moment is the highest and lowest in this flight condition as well, where the upwards moment is 2.93 times bigger than the downwards moment. Comparing the pressure distribution for this configuration in one graph, which is done in Figure 2.7, makes the difference more clear. It is seen that for this flight phase, the lowest force is achieved in the neutral position (N), where the maximum negative force is reached in the upwards deflected position (U) and the maximum positive force is reached in the downwards deflected position (D). It is expected that when the morphed trailing edge takes a position in between the +15 and -15 degrees, D and U respectively, the pressure distribution will take a shape in between those extreme pressure distributions. Which means that for a certain deflection, the force and moment can be 0. This position does not necessarily have to be the same, since the trailing edge can still produce a force, while the moments cancel out.

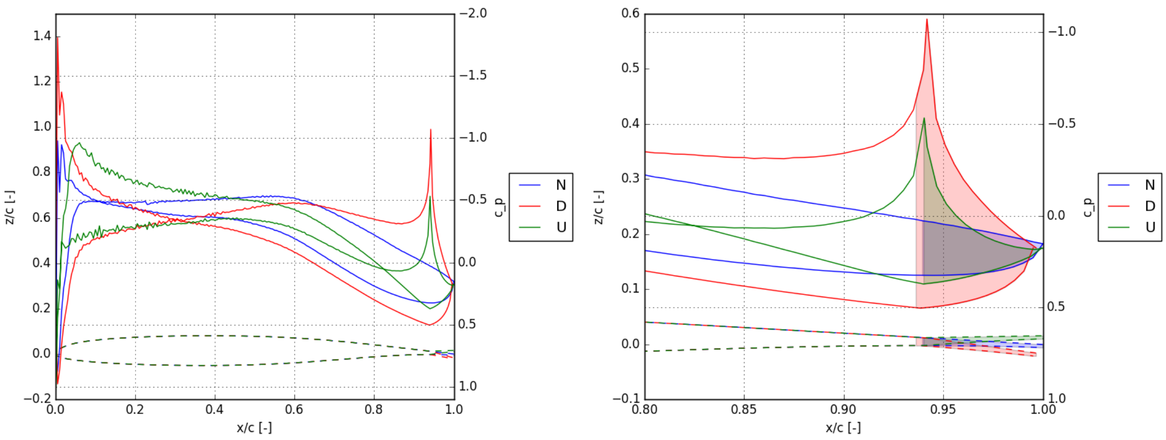

(a) Full (b) Zoomed

Figure 2.7: Pressure distributions from XFOIL for descent condition, morphing part Neutral (N), 15 degrees Down (D) and 15 degrees Up (U) position, $c_l = 0.17$, $Re = 29.9 \cdot 10^6$, $M = [0.6, 0.3, 0.6]$ respectively

Since the other flight conditions show a very similar behavior to the descent configuration, the same will apply for these conditions. One exception is the approach condition, where the extreme pressure distributions can be found in Figure 2.8. Here the loading is always positive and the moment acts in counterclockwise direction. Deflecting downwards will lead to a more rectangular distribution, where upwards still unloads the trailing edge with a small bump. In this configuration, it is expected that zero force and moment cannot be reached within the 15 degrees limits.

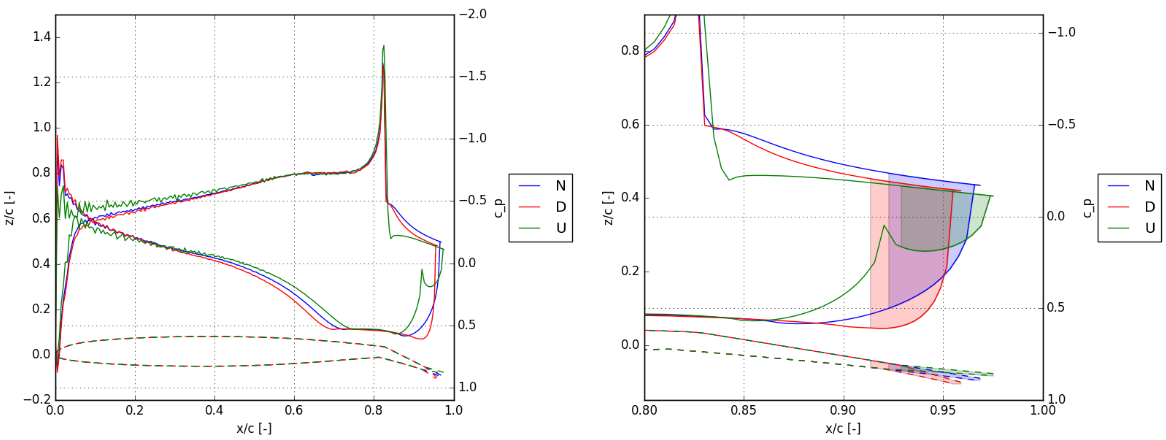

(a) Full (b) Zoomed

Figure 2.8: Pressure distributions from XFOIL for approach condition, morphing part Neutral (N), 15 degrees Down (D) and 15 degrees Up (U) position, $c_l = 0.594$, $Re = 16.8 \cdot 10^6$, $M = 0.197$

Another remark has to be made considering the pressure distributions. The peaks shown in the pressure distributions are mainly caused by a discrete deflection of the flap. Therefor a small investigation into the differences to discrete and continuous deflections has been performed. In Figure 2.9 the results are shown, where the same airfoil as for the complete Cessna Citation X analysis has been used. The discrete test is performed with a plain flap with the same size as the Citation Flap. The deflection is 30 degrees and a peak in the pressure distribution is shown around the hinge location. When the same deflection is applied over 300 sections (0.1 degree per section), a more continuous shape is formed, which is shown at the bottom of Figure 2.9. For the same lift coefficient, the pressure distribution shows a small bump for the continuous case, instead of a peak, and more rearward loading. The previous investigation with the discrete, plain flap type morphing trailing edge is therefor on the conservative side. If the actuator is able to produce continuous morphing, the loading estimation requires more in depth research between the differences in continuous and discrete pressure distributions.

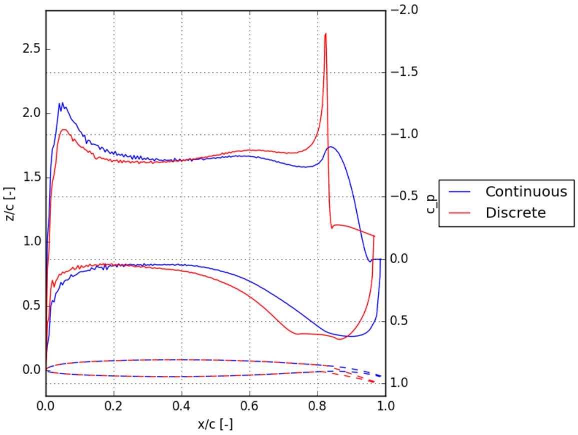

Figure 2.9: Pressure distribution from XFOIL for continuous and discrete deflection, $c_l = 1$, $Re = 16.8 \cdot 10^6$, $M = 0.197$

2.6. V-N DIAGRAM

In AAA, a V-n diagram is generated, in which the maximum load factors for maneuvering and gust loads can be found. The V-n diagram for the Cessna Citation X is found in Figure 2.10. In AAA, the V-n diagram is based on the Roskam method [32]. It shows that from stall speed, 70.6 m/s, to approximately 91 m/s, the V-n diagram is dictated by gust loads for positive load factors and maneuver loads for negative load factors. For higher velocities, the maximum load factor is determined by the maneuvers. The maximum positive load factor is 2.62 g, where the maximum negative load factor equals -1.00 g. The design load factors are dictated by the maneuver loads. This means that alleviating gust loads will not give large structural weight advantages. However, alleviating gust loads leads to an improvement in ride quality and an increase in the fatigue life.

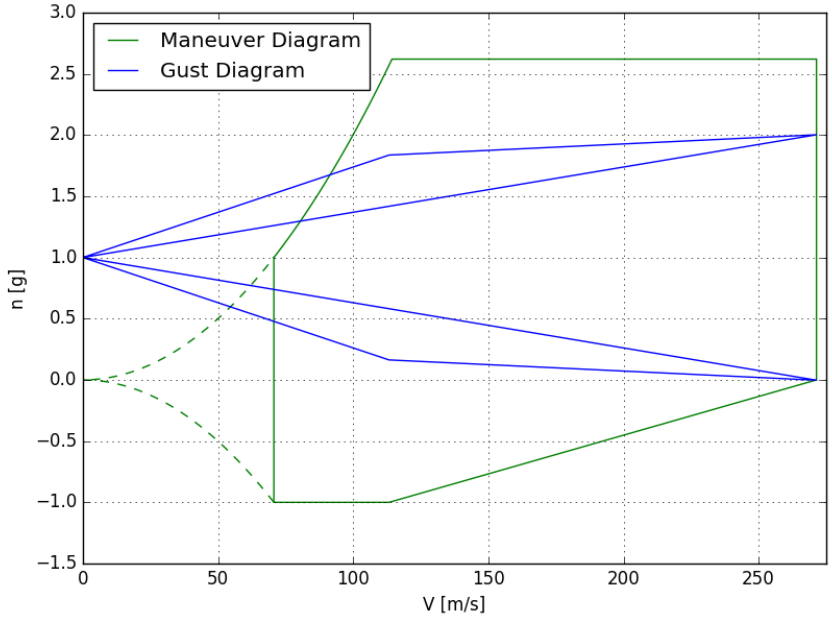

Figure 2.10: V-n diagram for Cessna Citation X from AAA

2.7. EXPECTED LOADING ON THE MORPHING PART OF THE FLAP

From Sections 2.2 to 2.4 the highest absolute values for the forces and moments are found in the descent flight configuration. The approximation of this loading is summarized in Table 2.8.

Table 2.8: Summary of the minimum and maximum loads expected on the morphing part of the flap, which are found in the descent flight configuration

Morphing Position	F_{morph} [N]	M_{pivot} [N · m]
Neutral	209.7	15.24
Positive	631.6	37.19
Negative	-253.4	-12.68

From Sections 2.5 and 2.6, ratios of the maximum and minimum forces and moments and the positive to negative load factor ratio can be found. These ratios can be used for the ratio of top bellow height to bottom bellow height, and are given in Table 2.9.

Table 2.9: Ratio of maximum to (absolute) minimum forces and moments and load factor ratio

	Ratio [-]
Force	1:2.49
Moment	1:2.93
Load Factor	1:2.62

3

PRELIMINARY DESIGN AND TEST SETUP

This chapter will give the preliminary design in Section 3.1. The preliminary design is broken down in the bellow design and the trailing edge design, which are given in Section 3.2 and Section 3.3 respectively. Section 3.4 concludes the chapter with the test setup design.

3.1. PRELIMINARY DESIGN

From the load estimation and V-n diagram the initial size distribution was set to 2.62:1. This size distribution is the ratio between the top bellow height to the bottom bellow height. Using this ratio and the thickness at 70% chord, the height for the top and bottom bellows can be determined, which are 26.27 mm and 10.03 mm respectively. In order to capture the dihedral of the flap and also allow for redundancy, it is chosen to divide the flap in spanwise direction in 5 separate actuators. This results in an actuator width of 334 mm. Since the flap measures 705 mm in chordwise direction and 30% from the trailing edge will be replaced by the actuation system, the length of the system will be 211.5 mm.

The number of bellows is another variable, the first design was made with 6 bellows on top and 5 on bottom, in order to create a nice wedge angle for the trailing edge to work with. The flap, with thicknesses as measured in Section 1.2 and dimensions as given above, is modeled in CATIA™. In the model, the bellow structure has been placed inside the flap around the 70% chordline, which is seen in Figure 3.1.

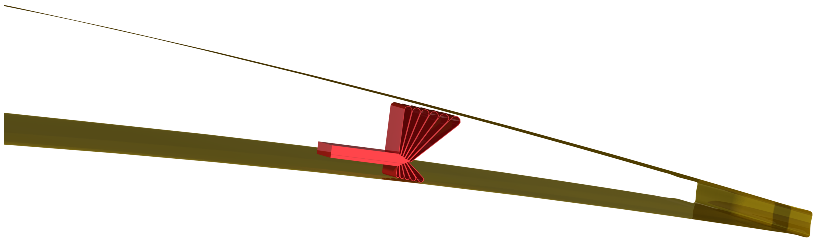

Figure 3.1: Preliminary bellow layout structure inside the flap with the bellows in red and the flap skin in brown showing approximately the trailing 50% of the flap

To simplify the model, the amount of bellows for the top and bottom parts are both set to 2, this is done for manufacturing reasons and represents the concept well. The working principle of the bellows is explained in Figure 3.2. The rest case with neutral, atmospheric pressure in both the top and bottom bellows is presented in Figure 3.2a. If the top or bottom bellows are inflated, the trailing edge is deflected, which is given in Figures 3.2b and 3.2c. The variable stiffness is achieved by increasing the pressure in the top and bottom bellows simultaneously. This is shown in Figure 3.2d.

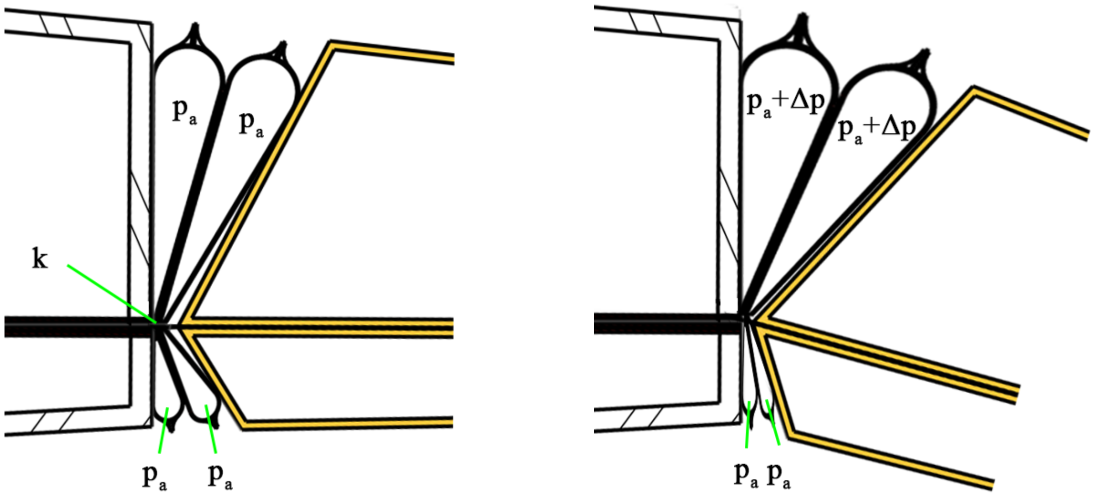

(a) Top and bottom neutral (b) Top pressure increased, bottom neutral

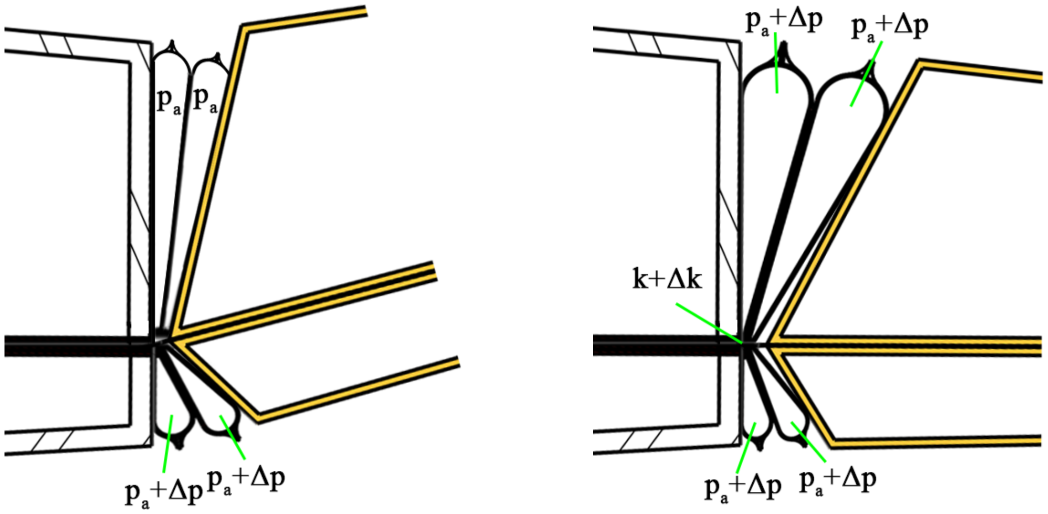

(c) Bottom pressure increased, top neutral (d) Top and bottom pressure increased

Figure 3.2: Actuator functionality explained, deflection with pressure p_{a} and $p_{\mathrm{a}}+\Delta p$ and increasing the stiffness to $\kappa+\Delta\kappa$, the trailing edge (yellow) is only partially shown

The initial design with two bellows which is used for production and testing is presented in Figure 3.3. Here the full flap is shown with the actuator in the trailing edge. More focus on the trailing edge is given in Figure 3.4. The flap is presented in the light blue color, the bellows in red, the trailing edge of the actuation system is represented in yellow and the L-stringers are aluminum grey.

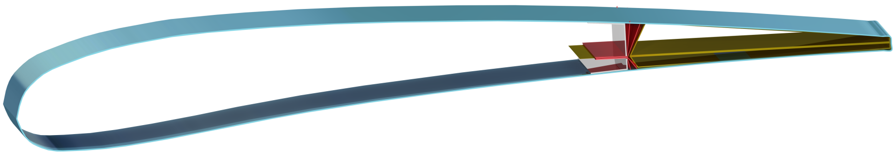

Figure 3.3: Preliminary design inside the flap with the bellows in red, L-stringers in grey, trailing edge in yellow and the flap skin in light blue

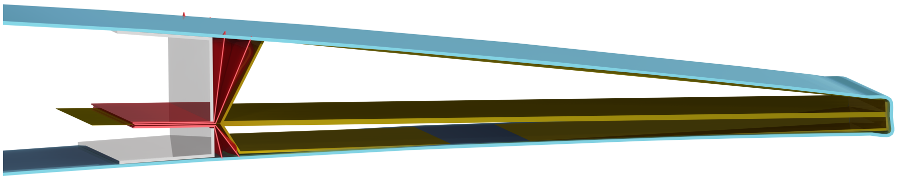

Figure 3.4: Preliminary design inside the flap showing approximately the trailing 35% of the chord, with the bellows in red, L-stringers in grey, trailing edge in yellow and the flap skin in light blue

The top and section view of the actuator are given in Figure 3.5. In the section view the two L-shaped stringers can be seen in the bottom which will be connected to the flap skin. The trailing edge will be connected to the skin as well. The bellows will be attached between the trailing part and the L-stringers.

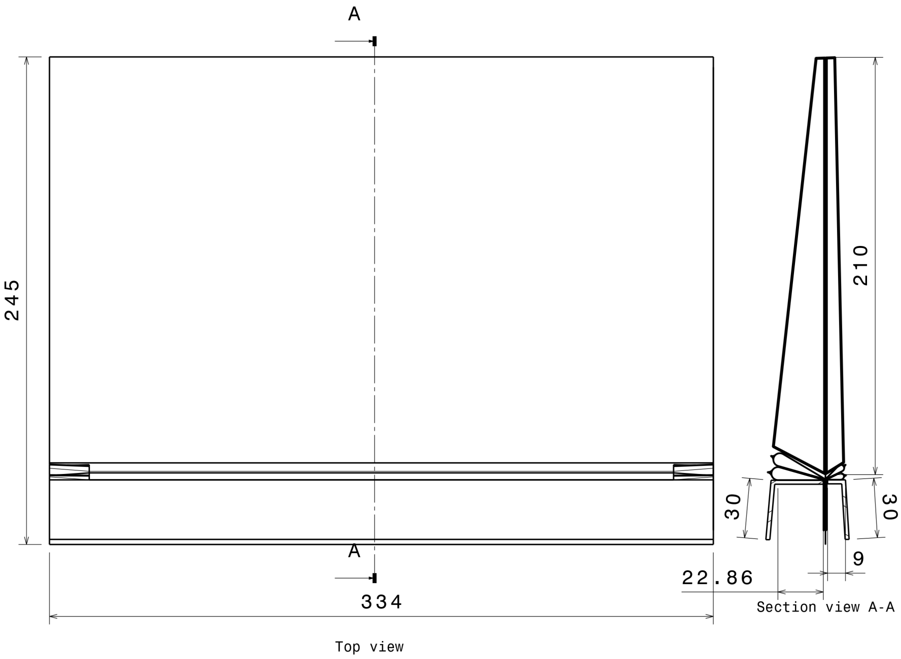

Figure 3.5: Top and section view of the actuator with dimensions in [mm] and [deg]

3.2. Bellow Design

The top view of the top bellows is given in Figure 3.6. The bellows are symmetric in the x-axis, where the width measures 334 mm and the cutout starts 20 mm from the end of both sides. Section views with dimensions for both bellows are given in Figure 3.7. The angle of the first bellow's flange equals 90 degrees. The angle of the second measures 90 degrees plus the 15.81 degrees from the first bellows thickness. The 15.81 degrees is not an arbitrary number, but follows from the radius and the height available for the bellow from the pivot point to the skin. The inner radius equals 1/8th inch, for which carbon fiber rods for production are available. The flange length is set to 1 inch, but can be made shorter/longer depending on the connection to the stringer. The thickness of the bellow is originally set to 6.7 mil (0.17 mm). This dimension was chosen to be as thin as possible in order to allow for the deformations by pressure. The University of Kansas also had 4 mil and 10 mil polycarbonate sheets available for this purpose, for which the design in Figure 3.7 can easily be adapted to.

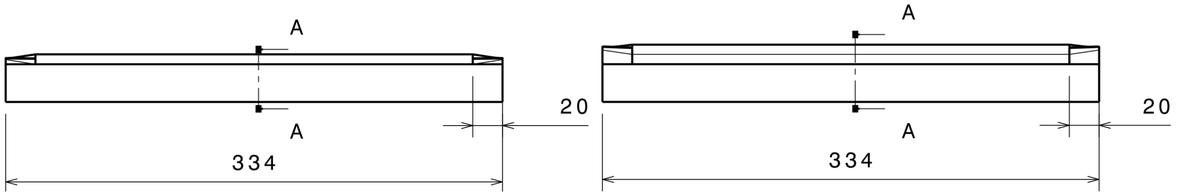

(a) Top bellow 1

(b) Top bellow 2

Figure 3.6: Top view of the preliminary design of the top bellows with dimensions in [mm] and [deg]

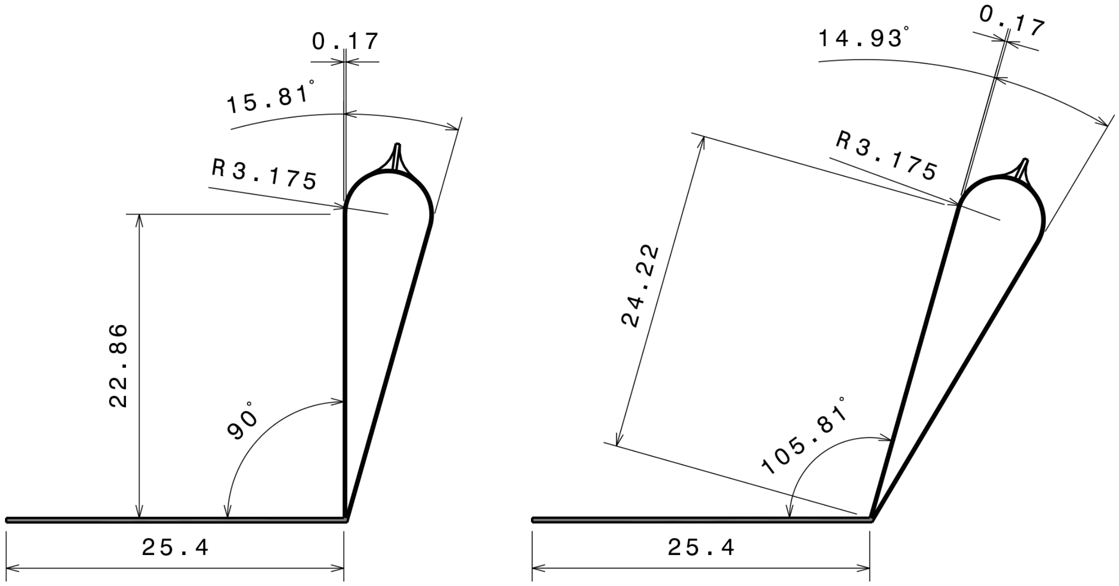

(a) Top bellow 1

(b) Top bellow 2

Figure 3.7: Cross-sectional view of the preliminary design of the top bellows with dimensions in [mm] and [deg]

Similar as the top bellows, the top view of the bottom bellows can be seen in Figure 3.8. They have the same width and cutout width as the top bellows. The sectional views of the bottom bellows are given in Figure 3.9. The flange length is the same as the top bellows. For bottom bellow 1 the angle is 90 degrees as well, to align nicely with the stringer it is attached to. The angle of the second bottom bellow is similar to the second top bellow: 90 degrees plus 25.84 degrees. The 25.84 degrees angle is found from the available bellow height and the radius, which is equal to 1/16th of an inch.

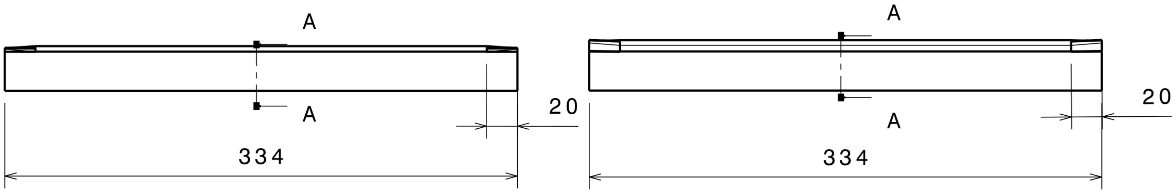

(a) Bottom bellow 1

(b) Bottom bellow 2

Figure 3.8: Top view of the preliminary design of the bottom bellows with dimensions in [mm] and [deg]

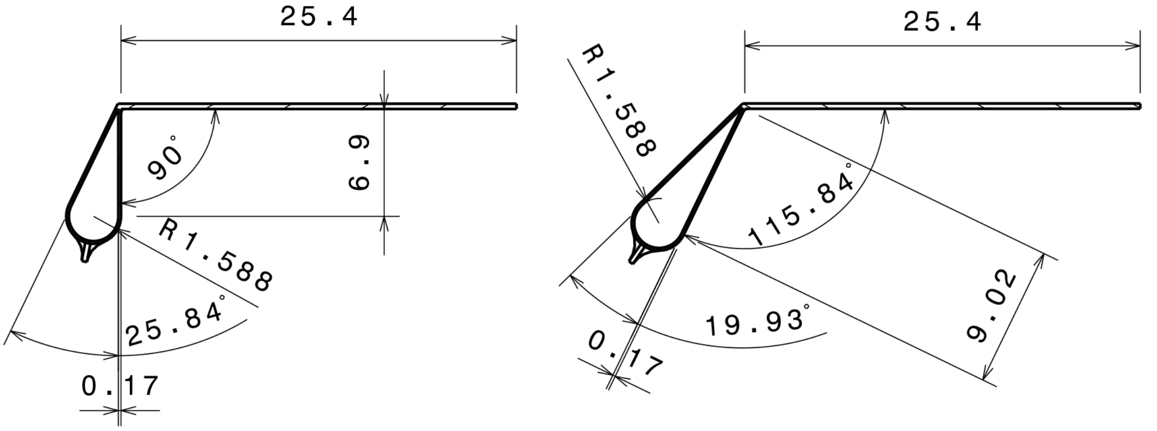

(a) Bottom Bellow 1

(b) Bottom Bellow 2

Figure 3.9: Cross-sectional view of the preliminary design of the bottom bellows with dimensions in [mm] and [deg]

3.3. TRAILING EDGE DESIGN

Since the main focus of the project is the structural properties of the actuator and not the aerodynamic properties, the trailing edge can be a simplified approximation of the airfoil shape. The trailing 30% of the airfoil has 4 corners, which are connected with straight surfaces in the model. Together with the wedge geometry at the pivot, the shape of the trailing edge is determined. The trailing edge front and side view can be seen in Figures 3.10 and 3.11 for the top and bottom respectively. It is chosen to have the middle sheet run all the way through to the trailing edge. The trailing edge is divided equally for the top and the bottom part, which is approximately 5 mm. For the top part, it is seen that the wedge angle is approximately 30 degrees, which is desired to make proper contact with the bellows. The other dimensions can be found in Figure 3.10. For the bottom, the wedge has a similar angle. Looking at the cross section of the bottom bellows, one will notice that this does not match the angle of the two bellows together. This means that the bellows will slightly be compressed, to make the connection as tight as possible. The thickness of the polycarbonate trailing edge sheets is 30 mil (0.74 mm). The inner sheet is a simple rectangle, which measures at least 334 mm in width. The length is at least the 210 mm from the middle of the trailing edge plus the 25.4 mm of the flange length, which equals 235.4 mm. The thickness of the inner sheet is as thin as possible, since this determines the stiffness of the trailing edge, which the bellows have to counter for deflections.

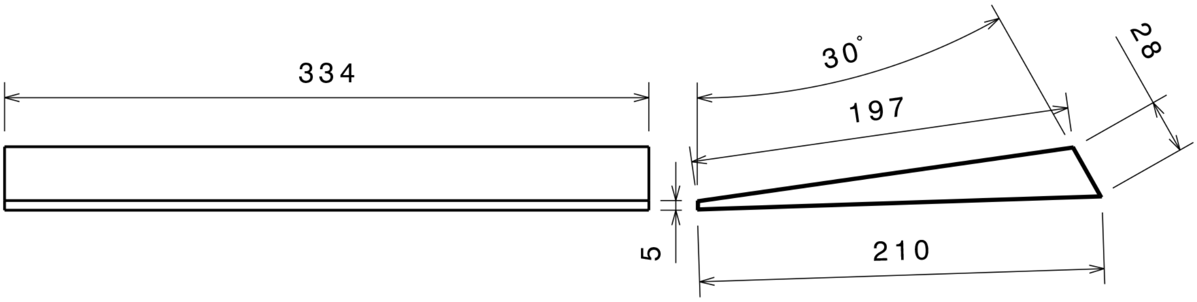

Figure 3.10: Front and side view of the top part of the trailing edge with dimensions in [mm] and [deg]

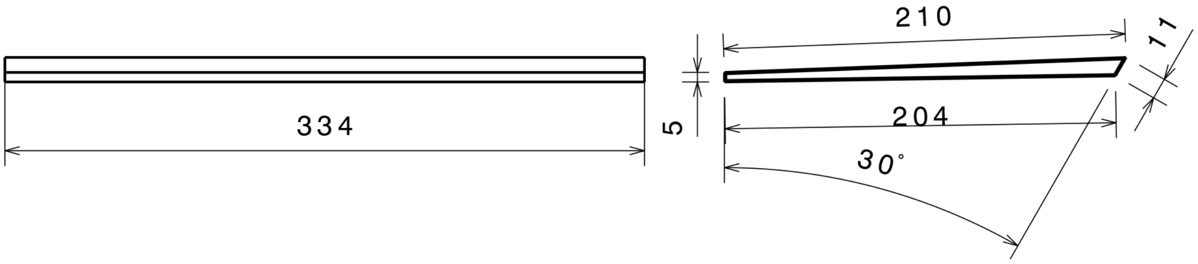

Figure 3.11: Front and side view of the top part of the trailing edge with dimensions in [mm] and [deg]

Looking purely at the wedge angle of the trailing edge in connection to the spar, limitations in the maximum deflection can be found. The current wedge has a 30 degrees angle at both the top and the bottom. The limitations are illustrated well in Figure 3.12. The maximum deflection upwards is restricted by the angle of the top part of the trailing edge, while the maximum downwards deflection is restricted by the bottom wedge angle. The angle will be smaller than 30 degrees, since the bellows in between will occupy some space as well, however it is expected that this is negligibly small since the bellows can fully deflate.

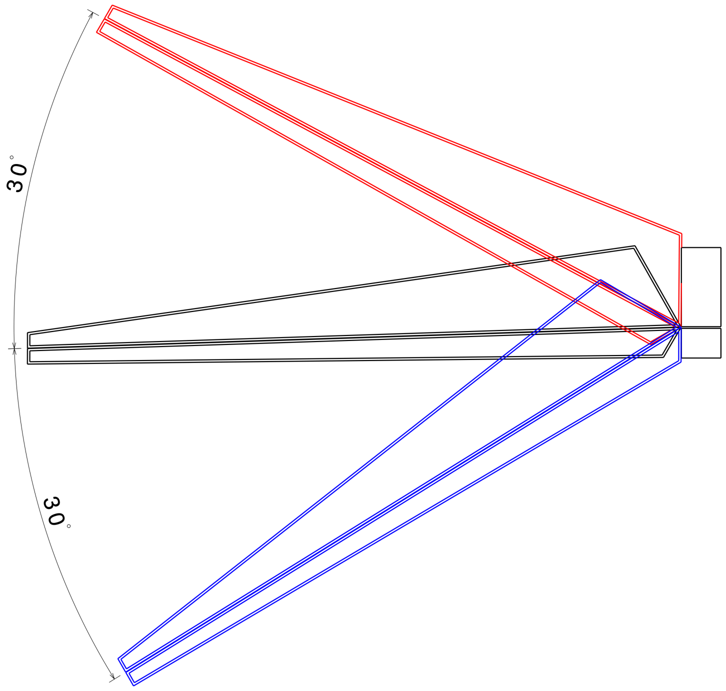

Figure 3.12: Maximum deflection due to wedge geometry visualized, maximum positive deflection in blue, maximum negative deflection in red

3.4. TEST SETUP

It was chosen to model one of the actuators instead of rebuilding the whole flap system. The L stringers are replaced by solid aluminum bars, which measure 0.5 in (12.7 mm) in width. The height of the top bar is 1 in (25.4 mm) and the bottom bar measures 0.375 in (9.525 mm) in height. The resulting design is shown in Figure 3.13.

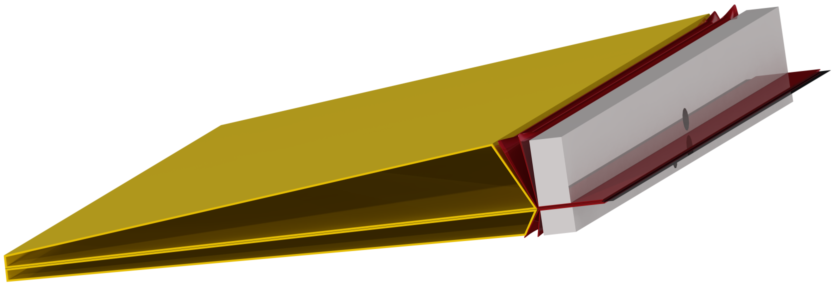

Figure 3.13: Rendering of the test object with the bellows in red, spars in grey, trailing edge in yellow and the inner sheet in black

The bars used for the top and bottom are also used to build a test stand. The width of the stand has to be slightly bigger than the test object, such that it is free to move. The test stand has to be stiff enough to not influence the test results. The bolts used to screw the assembly together are also used to attach the test object to the test stand. The complete test setup can be seen in Figure 3.14. The test stand is green, and the test object has the same colors as in Figure 3.13. The bars on the bottom of the test stand are connected by using L-connections, which are shown in a lighter green. The smaller, top bar is screwed to the vertical bars, making a rigid connection. In the bar on top a hole with the same diameter as the bolts in the test object is made on one side. The other side has a sloth with the same diameter. This is chosen, because the alignment is not perfect and to make the test stand universal, such that multiple test objects can be used on the same test stand. The hole will prevent movement in the spanwise direction, while both connections, the hole and sloth, will prevent movements in chordwise and vertical direction. The rotations in the systems around the x, y and z-axis are also blocked by this connection. What also can be seen in Figure 3.14, are the two staggered holes in the test object. The reason for staggering the holes, is to make the tubes easier to attach. The holes are connected to gauges, valves and pumps, to control the pressure in the system.

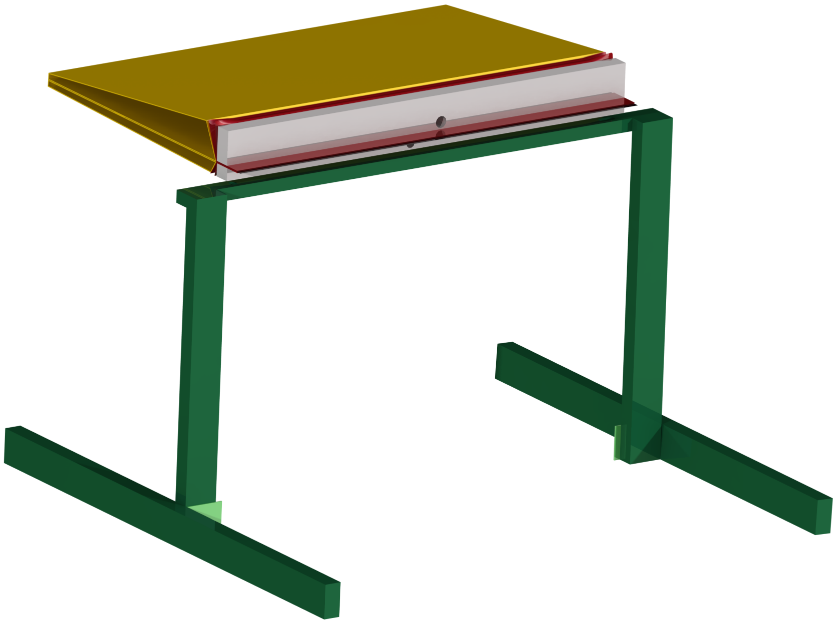

Figure 3.14: Rendering of the test setup where the test object from Figure 3.13 is mounted on top of the green test stand

4

PRODUCTION OF THE ACTUATOR

With the preliminary designs, the actuator can actually be produced. The materials used in the production are given in Section 4.1. The production of the individual parts is described in Section 4.2. The assembly, made from the previously described parts, is found in Section 4.3. In Section 4.4 the weight estimations and measurements are given. Finally, the issues encountered during production and testing are described in Section 4.5.

4.1. MATERIAL

The bellows are made from polycarbonate. The properties of polycarbonate are given in Section 4.1.1. The spars/stringers are made of aluminum, for which the properties are given in Section 4.1.2. According to Jane's All the World's Aircraft [29], the flap is built from Kevlar® and graphite composites. Upon inspection of the flap, there is no reinforcing inner structure and the loads are carried by a skin structure only. The properties for Kevlar® and graphite composites are given in Section 4.1.3

4.1.1. POLYCARBONATE

Polycarbonate is a high strength, low weight thermoplastic polymer. The material has a low density, low Young's Modulus but relatively high yield and tensile strength. The properties of polycarbonate are given in Table 4.1. In here it is seen that indeed the density is low, while the ultimate tensile strength is relatively high for polymers. Together with the low stiffness, this makes the material suitable for the application of the bellows. The University of Kansas has a supply of polycarbonate sheets with different thicknesses, ranging from 4 mil (0.1016 mm) to 30 mil (0.7620 mm). The specific strength of polycarbonate equals 0.052 - 0.060 MPa/(kg/m^3).

Table 4.1: Material properties of polycarbonate [33]

Property		Value
Density	[kg/m^3]	1200
Yield Strength	[MPa]	62.1
Tensile Strength	[MPa]	62.8-72.4
Young's Modulus	[GPa]	2.38

4.1.2. ALUMINUM

For the spars, aluminum bars with two different cross sections have been ordered. Aluminum is still one of the most used materials in aeronautical applications, although composites are used more in new deliveries. Since for aerospace applications different alloys are being used, the properties for three different, common aerospace aluminum alloys are presented in Table 4.2. It can be seen that the alloy with the lowest density is the 6061-T6. However, this alloy has lower yield and tensile strength. The specific strengths are 0.175, 0.115 and 0.204 MPa/(kg/m^3) for the 2024-T3, 6061-T6 and the 7075-T6 respectively, which is a factor 2-3 higher compared to the polycarbonate. The Young's Modulus for aluminum is considerably higher than the polycarbonate and is close to 70 GPa for all alloys.

Table 4.2: Material properties of typical aircraft aluminum grades [33]

Property	Alloy:	2024-T3	6061-T6	7075-T6
Density	[kg/m^3]	2770	2700	2800
Yield Strength	[MPa]	345	276	505
Tensile Strength	[MPa]	485	310	572
Young's Modulus	[GPa]	72.4	69.0	71.0

4.1.3. KEVLAR® AND GRAPHITE COMPOSITES

Since the flap has been made from Kevlar® and graphite composites, the properties are presented in Table 4.3. The skin is built with layers of graphite composite with a Kevlar® coating. To reproduce the leading edge, it is preferred to use the same materials as the original flap. The specific strength for Kevlar® ranges from 2.50 - 2.85 MPa/(kg/m^3). For graphite, this is considerably lower where it ranges from 0.00807 - 0.0388 MPa/(kg/m^3). However, one should note that pure graphite is a ceramic material, graphite composites consist of graphite with a resin. The mold is for example made from woven graphite sheets with West Resin®, which is an epoxy resin with high strength properties.

Table 4.3: Material properties of Kevlar® and graphite [33]

Property	Material	Kevlar®	Graphite	
			Extruded	Isostatically molded
Density	[kg/m^3]	1440	1710	1780
Yield Strength	[MPa]	n/a	n/a	n/a
Tensile Strength	[MPa]	3600-4100	(13.8-34.5)	(31-69)
Young's Modulus	[GPa]	131.0	11.0	11.7

4.2. PARTS

This section is split in four smaller sections, each describing different parts in the production process. Section 4.2.1 will describe the production of the top and bottom bellows, which is followed by the production of the spar in Section 4.2.2. The leading edge, although not produced in this thesis, is discussed in Section 4.2.3. Finally, the trailing edge production is discussed in Section 4.2.4.

4.2.1. BELLOWS

The bellows are made of polycarbonate, which are thermoplastic polymers. The polycarbonate sheets available at The University of Kansas have thicknesses of 4 mil (0.1016 mm), 6.7 mil (0.1702 mm) and 10 mil (0.2540 mm). The 10 mil is too stiff for the purpose of the bellows, so the bellows are made of 4 and 6.7 mil polycarbonate. The polycarbonate is heated on top of a carbonfiber rod with 1/8 inch radius for the top bellow and 1/16 inch radius for the bottom bellow. The polycarbonate will then drape down and after a brief moment, it will be removed from the heater. With the press the bellow is closed at the bottom and the flange is created. The draping and usage of the press is shown in Figures 4.1a and 4.1b. The flange of the bellow is then glued with acrylics. The bonding process is about 24 hours, after this time period the excessive material is cut away. It was chosen to start with excessive material which could be cut to the proper dimensions. For the top bellows a sheet of 400 by 150 mm is used, where the bottom bellows are made from a smaller sheet: 400 by 125 mm. This is easily cut down to the required 334 mm and offers sufficient material in the bellow and flange circumference.

After cutting the excessive material away, a bellow with two openings on either side is left, where the flange has been glued and made airtight. The openings on the sides are then glued together and with the help of clamps they are made airtight in the 24 hours bonding process. A supply of bellows was made, since the production process took over 48 hours. In case of issues in the test phase, the supply would prevent any further delays.


(a) Draping process
(b) Forming the angle with the press

Figure 4.1: Production processes of the bellows

4.2.2. SPAR

The spars representing the L-stringers are made of aluminum bars, where the top bar measures 0.5 in (12.7 mm) by 1 in (25.4 mm) in cross section and the bottom bar measures 0.5 in (12.7 mm) by 0.375 in (9.5 mm). The bars had to be sawed in the right length for the application to the actuator. The desired length is 334 mm, equal to the width of the bellows. The bar is sawed with the horizontal bench saw after which the holes are drilled. The holes are drilled on the 0.5 in side all the way through, to connect the spars with bolts and nuts. The chosen hole diameter was 0.25 in (6.4 mm). The holes are first drilled on the top part only, after which the bottom part was clamped to the top part for the alignment of the holes.

Once the holes are drilled for the bolts, the holes for the air had to be made. The diameter for these holes are determined by the size of the male tube connection which will be screwed in the hole. For the top part, a 1/8th NPT (National Pipe Thread) tube was available at The University of Kansas, which has a diameter of 0.405 in (10.3 mm). Since this tube would not fit on the bottom part a smaller tube had to be found. One tube was found with M8-1.00 (Metric threading system) threading, which required a hole diameter of 8.25 mm. After the hole has been drilled, the holes are threaded with the according tap and die set for the specific thread.

4.2.3. LEADING EDGE

The molds produced during this thesis can be used to recreate the leading edge. The female molds are directly made from the original flap and follow the curvature well. The top and bottom can be recreated separately and then joined afterwards. The technique to create the leading edge can be similar to the technique of making the mold. Woven graphite sheets can be laid up to the mold, after which resin has to be added to harden and strengthen the material. This is a quick process, which uses the same materials as the molds. The Kevlar® coating of the flap can be added to fully recreate the flap with similar material properties.

One should note the purpose of the leading edge which will be created. If it is structurally only, it will be easy. However, if the purpose will be to test the flap and actuation system aerodynamically, the surface has to be as smooth as the original flap. Any imperfection will lead to flaws in the test results.

4.2.4. TRAILING EDGE

The trailing edge consists of three separate parts, the top part, the bottom part and the sheet in between. The top and bottom part are produced similarly, while the inner sheet is the easiest part to produce and does not require many steps.

The top of the trailing egde is made from 30 mil (0.762 mm) thick polycarbonate sheet. The sheet has to be cut down to 334 mm in width and 440 mm in length. Then the press is used to create the angles in the sheet at 5 mm, 202 mm and 230 mm, which are basically the angles from Figure 3.10 starting at 5 mm with the top left corner and continuing in clockwise direction. The top trailing edge part with the order of the corners in which they are being formed in the press can be seen in Figure 4.2. This way the shape of the trailing edge is formed easily and the trailing edge only needs to be bonded together using tape or an adhesive. The bottom is produced similarly, with minor differences in the dimensions. The sheet has to be cut down to 334 mm by 430 mm. The angles from Figure 3.11 will then be created by the press at 5 mm, 209 mm and 220 mm, starting from the bottom left corner going counterclockwise.

For the tests the inner sheets are made of 4 mil (0.10 mm) and 6.7 mil (0.17 mm) polycarbonate sheets.

They are simply cut to the required dimensions of 235.4 mm by 334 mm.

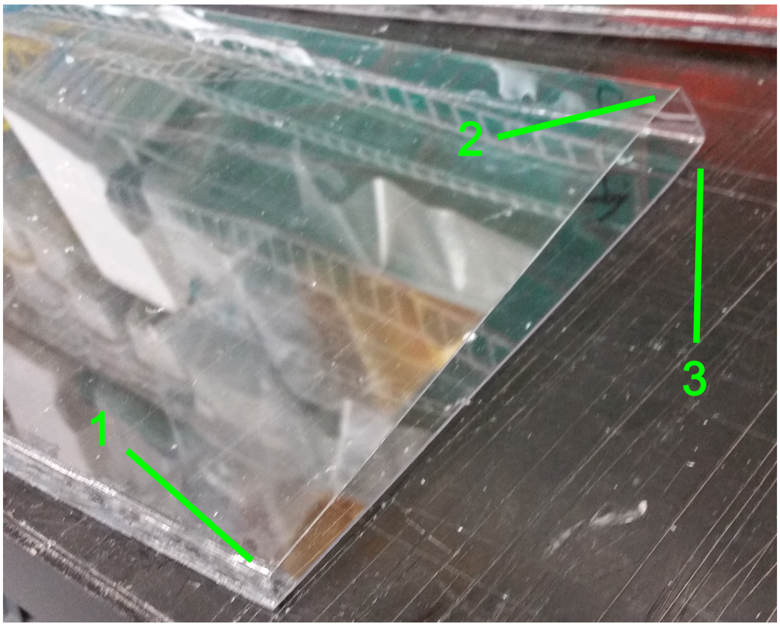

Figure 4.2: Top of the trailing edge with order of the corners in which they are formed by the press

4.3. ASSEMBLY

The assembly is one process and will describe the steps taken to get from all parts to the final actuator design. For the actuator assembly, the required parts are given in Table 4.4.

Table 4.4: Bill of material for the assembly of a single actuator

Part	Top	Bottom
Bellows	2	2
Spar	1	1
Trailing edge	1	1
Inner sheet	1	
Bolts (1/4th in)	2	
Washers	4	
Nuts	2	

First the bellows will be attached to the appropriate spar. This is done by first creating a hole in the flanges of the bellows. The corner of the flange has to be as close to the corner of the spar. When the bellows are on the bolt, the first three out of four layers of the bellows are punctured. This is done to have the air flow through the spar to the first bellow and through the spar and first bellow to the second bellow. This is shown in Figure 4.3, where the layers which have to be cut through are numbered.

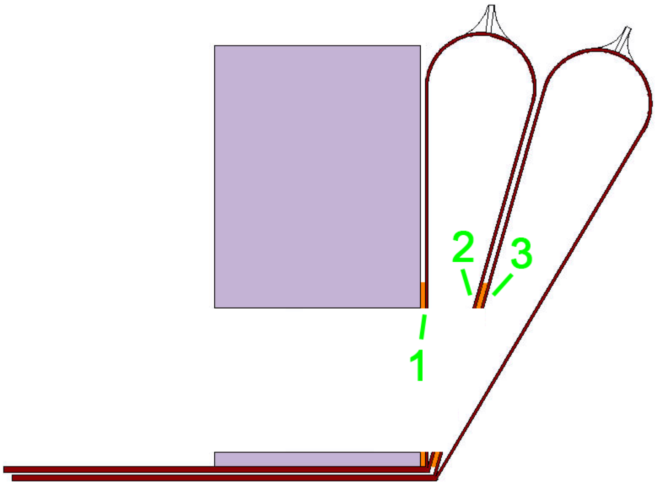

Figure 4.3: Layers of the bellows which need to be cut (numbered) and location where adhesive has to be applied for air tightness (orange)

After the holes are made with approximately the same diameter as the hole in the spar, the first bellow is glued to the spar and the second bellow is adhered to the first bellow. This bond is made using Permatex® Black Plastic Welder. This is an epoxy adhesive and is able to bond the aluminum with the polycarbonate. Using q-tips, the epoxy is applied around the holes on both sides of the surfaces which are being attached, which is shown in Figures 4.3 and 4.4. Once the adhesive has been applied, the bellows are clamped to the aluminum such that the bond can cure. This is done for the top and bottom bellows separately.

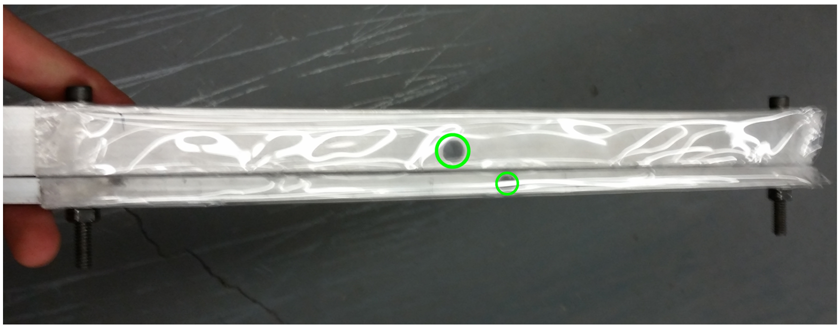

Figure 4.4: Locations where the epoxy adhesive is applied to the spar and bellows using q-tips

For the trailing edge, the top, bottom and inner sheet have to be assembled. This can be done using adhesive, which has to cure as well. For the test it was chosen to put the trailing edge together using tape. After this, the trailing edge can be attached to the spars and bellows, which is done by making holes in the inner sheet, aligning the trailing edge as close as possible to the bellows. Once the holes are made, the assembly is screwed together, using the bolts, nuts and washers.

The test stand is made from the same aluminum bars as the spars. The parts are sewed in the proper dimensions using the horizontal bench saw. As connecting element, an L-stringer is sewn in two small parts with a width of 1 in (25.4 mm). This is done to connect the horizontal stabilizing bars with the vertical bars. The top is made of the 3/8th in (9.53 mm) aluminum bar, such that the same bolts could be used to attach the test item to the test stand. Holes are drilled in all bars and L-Stringers with a 1/4th in (6.35 mm) diameter drill, after which they are connected using bolts, nuts and washers. For the test stand, the cross sections of the aluminum bars and connectors which are used are given in Table 4.5. These are connected by using six bolts with 1/4th in diameter, 12 washers and 6 nuts.

Table 4.5: Cross section dimensions for the aluminum bars and connectors used in the test stand

Part	Amount	Cross Section
Horizontal aluminum bars	2	12.7 mm by 25.4 mm
Vertical aluminum bars	2	12.7 mm by 25.4 mm
Hanging aluminum bar	1	12.7 mm by 9.53 mm
L-shaped connectors	2	25.4 mm by 2 mm

The system also has to be attached to pumps for supplying the air pressure. For this reason, two vacuum pumps are being used. It was chosen to supply the pressure with two separate pumps such that the pressure in both systems could be arranged individually. However, it is not necessary to use two pumps, instead a splitter tube could have been used as well. The pumps are connected to valves, which controlled the air pressure. The end of the valves are wired to the 1/8th NPT and M8-1 tube, which are screwed to the test object. For all the screwed connections, plumber tape has been used to ensure the air tightness of the wiring. The connection of all wires, tubes and pumps are strengthened with hose clamps. The tested actuator with connected tubes and wiring is shown in Figure 4.5. The wires leave the picture in the bottom right, the valves and pumps are not shown in this picture. Note that the tested object consists of two top sides of the actuator instead of a top and bottom, the reason for this will be explained in Chapter 5.

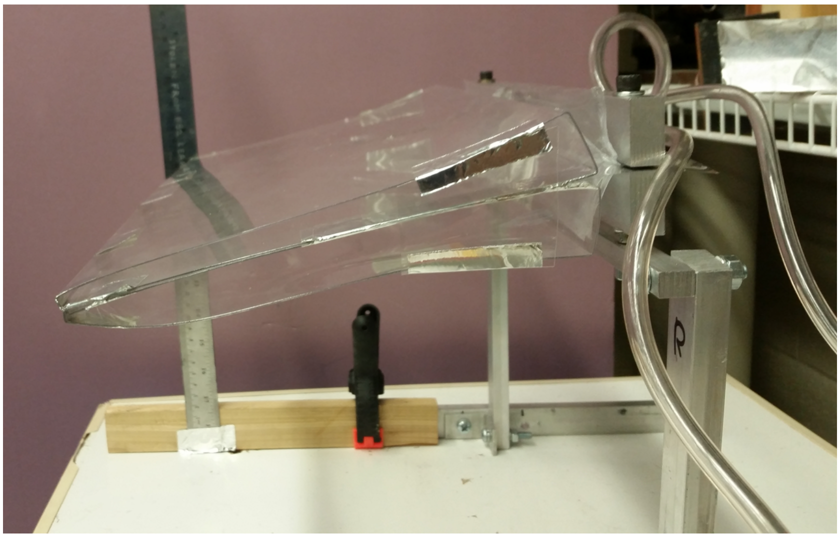

Figure 4.5: Actuator attached to the test stand and connected to the tubes and wiring

4.4. WEIGHT MEASUREMENT AND ESTIMATION

Since the density of the materials and the volume of the used materials is known, a weight estimation can be made for the individual parts. The weight of the trailing edge has been measured, since this is necessary in the differential equation for the torsional spring damper system.

The weight of the trailing edge (with two top trailing edges, as used in the test setup) with a 4 mil inner sheet equals 330 grams. The second tested trailing edge with a different inner sheet, namely the 6.7 mil sheet, equals 342 grams. This weight increase is most likely not only caused by the inner sheet, since the volume of polycarbonate only increased by approximately 5500 mm^3. With the density of polycarbonate, the weight increase by the inner sheet is 6.6 grams, which is half of the measured weight increase. The other weight increase is expected to come from additional tape being used.

To estimate the weight of the actuator and the flap, some assumptions have been made. These assumptions are as follows:

- The L stringers are made from aluminum and have a 2 mm thickness
- The skin of the flap consist of 2 mm graphite with 1 mm Kevlar® coating
- The volume of the parts is equal to the volume estimation in CATIA™

- The weight of the adhesive is negligible
- The weight of the tracks and actuation linkages is not included in the calculation

The estimated weight of the parts, the assembly and the flap is then found in Table 4.6. Note that the flap weight is just a rough estimation, since it is made of graphite composites and not of pure graphite. For the bellows a thickness of 6.7 mil (0.17 mm) is taken and the inner sheet has 4 mil (0.10 mm) thickness. The weight for a single actuator with two bellows on top and bottom equals 475 grams. Since there are five actuators in a flap, the actuator would increase the weight of the flap by 2375 gram, which is 18.9 % of the estimated flap weight. This is excluding the tubes, wires and pumps. As can be seen, the trailing edge and the stringers are the heaviest part of the actuator, contributing for 93.7 % of the actuator weight. If a more in depth optimization of the trailing edge and the L-stringers is performed, the actuator weight can be brought down significantly. Other weight savings can be achieved by integrating the trailing edge into the flap skin.

Table 4.6: Weight estimation of the parts and flap

Part	Volume [cm^3]	Material	Density [g/cm^3]	Weight [g]
Top Bellow 1	8.0	Polycarbonate	1.20	9.5
Top Bellow 2	8.2	Polycarbonate	1.20	9.8
Bottom Bellow 1	4.4	Polycarbonate	1.20	5.2
Bottom Bellow 2	4.6	Polycarbonate	1.20	5.6
Top Trailing Edge	111.6	Polycarbonate	1.20	133.9
Bottom Trailing Edge	108.7	Polycarbonate	1.20	130.4
Inner sheet	8.1	Polycarbonate	1.20	9.8
Top L-stringer	36.3	Aluminum	2.80	101.5
Bottom L-stringer	24.7	Aluminum	2.80	69.2
Flap (graphite part)	5018.0	Graphite	1.78	8932.0
Flap (Kevlar® part)	2509.0	Kevlar®	1.44	3613.0

From Table 4.6 it follows that the trailing edge weight with two top trailing edge parts is estimated to be 277.6 grams, which is 52.4 grams lower than measured. It is assumed that the aluminum tape used for the assembly is contributing for this difference. Aluminum tape is not optimum for weight considerations. It is expected that the measured weight of the trailing edge will decrease if acrylics or other tape is being used.

4.5. PRODUCTION AND TESTING ISSUES

Since manual labor is involved in the production of the actuator, imperfections can be found. Also, other issues were found in the production of the bellows and the actuation system. The thickness of the bellows gave some issues, which are discussed in Section 4.5.1. Since the dimensions in the drawings have a precision to a hundredth of a mm, this is very hard to manually produce. The complications for this are discussed in Section 4.5.2. Working with the Permatex® Black Plastic Welder required some special care and induced implications, which are given in Section 4.5.3. The issues which became apparent during the test phase, for which the results are given in Chapter 5, are given in Section 4.5.4.

4.5.1. THICKNESS ISSUES

Since the chosen thickness of the bellows was 0.10 and 0.17 mm, the material is very thin. This caused some implications in the production. For the closeout, it was chosen to seal with an iron. This worked out well for a bellow with thickness of 10 mil (0.254 mm). However, for the smaller thickness, which is used for the bellows, ironed seals caused the bellow to wrinkle. Since these wrinkles were undesired, another method of sealing had to be chosen. The other method was using the acrylics as adhesive as described in Section 4.2.1. The use of an iron was still applied on a smaller scale, where the top corner of the closeout was sealed, as the clamps and the acrylics were not able to seal this perfectly.

Other problems with the thickness were the holes in the bellows, which had to go all the way through, except for the second polycarbonate layer in the second bellow, which is shown in Figure 4.3. It happened multiple times that, with creating the holes, the last layer was penetrated as well, especially for the bottom bellows. This required the replacement of the second bellow and sometimes both bellows. The bottom bellows were more difficult to penetrate. Because the dimensions of the holes were much closer to the top and bottom of the spar, it required a higher precision.

4.5.2. DIMENSIONAL ISSUES

As discussed in the introduction of this chapter, the designs in Chapter 3 show dimensions of hundredths to even thousands of millimeters. For the radii of the bellows this was not a big problem, since this dimension is depending on the rods used in the heater, for which the dimensions were in inches. However, the bellow height gave more difficulties, which according to Figure 3.7 had to be 26.055 mm for the first top bellow and 27.395 mm for the second top bellow. It was already difficult to create accuracy up to 2 mm, so the thousands of millimeters were next to impossible to achieve. The reason why they are included in the designs, is the significant figures. Since some dimensions are converted from the metric system and imperial system back and forth it was chosen to keep the dimensions to a thousand of millimeters accuracy in the designs. This also applied to the bellow angle, where the 90 degree angle was pretty easily achieved with the press, the 105.81 degree angle proved to be more difficult. However due to the flexibility of the bellows, the angle was approximately achieved in the assembly process, as the bellows were assembled close together.

The problems with the dimensions were even bigger for the bottom bellows, since the bellow height was only 8.488 mm for the first and 10.608 mm for the second. With the press, it was very difficult to create dimensions of this size and it proved to be difficult to achieve this exact height even more. The bottom bellows had the same problems with the angles as the top bellows. The 1 in (25.4) mm flanges and 334 mm width, with 20 mm closeout regions on both sides, were more easily achievable for the top and bottom bellows. Some deviations might have been possible due to manual labor (cutting), however in general these dimensions were a much better approximation than the bellow heights.

For the trailing edge, some dimensional difficulties were present as well. To create the first corner with the press at 5 mm from the edge of the 30 mil (0.762 mm) sheet, required the most precision and due to the press it was not easy to get the exact dimensions. It was hard to achieve the exact angles, which also had to do with the springback of the material after using the press.

After the assembly, the trailing edge angle appeared to be close to the 30 degrees which was given in the design. However, the bellows did not make proper contact to the trailing edge. The chosen solution was to make the trailing edge angle a little smaller to induce better contact between the trailing edge and the bellows. The smaller trailing edge angle was achieved by reducing the 209.9 mm inner length slightly, pushing the second corner (see Figure 4.2) forward. The trailing edge was also supposed to be as close to the spar as possible, however due to imperfections in the assembly, up to 2 mm of distance was seen between the tip of the wedge and the spar.

4.5.3. ADHESIVE ISSUES

Application of the Permatex® Black Plastic Welder required high precision. The mixing process was made fairly easy, where the tubes made sure the mixing quantities were very close to the optimum. After the mixing, the application to the bellows was done by using q-tips. The application had to be performed pretty quickly, as the viscosity of the adhesive went down after the mixing process. Even though it was tried to apply the adhesive in a perfect circle, the time pressure made it very difficult. The amounts of applied adhesive also varied per surface, creating asymmetries in the assembly.

If too much epoxy was applied, the stiffness of the bellows around the holes went up significantly. Since the adhesive has a higher stiffness, the deformation around the holes was affected. Especially near the holes, the bellows were very hard to fully inflate, such that the main deformation occurred in the outer parts of the bellow.

It was also found that the adhesive clogged the air supply to the bellows. During the curing process clamps were used, which pushed the epoxy to the edge of the holes. This caused the bellows to not inflate at all. When the holes were tried to be unclogged with needles, the needles could puncture the last bellow layer easily due to the thickness. When the last layer of the bellow got penetrated, both bellows had to be replaced. This is a very time consuming process.

As discussed before, the adhesive made the bellows a lot more stiff. When the bellows are inflated, the bellows are trying to become more circular. Because the stiffness around the holes prevented this, the polycarbonate ruptured around the area where the adhesive is bonded. This hole was very hard to fix and often led to replacing both bellows.

Other issues with the adhesive considered the acrylics, which is applied to the closeout and the flanges of the bellows. Once the bond cured after 24 hours, it appeared that the air tightness of the bellows was often not achieved. The bond is supposed to be strong and airtight, however it is the first thing to fail when the bellows are pressurized. Even with low pressures, air tightness could not be fully achieved. Due to time constraints, it could not be made fully airtight, so it was accepted that some air was able to escape. This could be caused by the method of applying the acrylics, which is done with q-tips. It was seen that the q-tips degraded when the acrylics is applied, which might contaminate the bond.

The air tightness might also have been a problem due to the adhesive bond around the holes, since the bonding surface is very small especially at the bottom. As an additional test object, the hole for the air supply was tapered towards the bellow. This made the surface a bit bigger, making it easier to apply the adhesive. However, adding taper to the holes still did not guarantee air tightness. Any leaking air is not desired, so to solve this problem in future designs the cause of the leak has to be found. This can be done by applying small particles (powder) to the air to locate the source of the leak(s). When the source is traced, a full conclusion on the cause and suggestions for improvement can be made.

4.5.4. TESTING ISSUES

During testing issues were found as well. The first failure occurred during the deflection speed test. When the speed was tested and the oscillations increased, the trailing edge dropped down at one point. This was caused by the inner sheet connection, where just a small area was taped to the top and bottom part of the trailing edge. This connection failed, making the top and bottom slid off the inner sheet of the trailing edge. This was solved by using more surface for the connection between the three elements of the trailing edge.

Another failure became apparent when the trailing edge was not perfectly connected to the bellows anymore and the assembly was disassembled for inspection. The inner sheet sheared out at the locations of the bolts, which can be seen in Figure 4.6. In Figure 4.6a the failure just enlarged the hole at the bolt location, but for Figure 4.6b the sheet completely ruptured. This failure is caused by the bearing forces, the loads induced by the deflections are not transferred to shear forces into the flanges of the bellows, but only to the bearings. The inner sheet is not capable of withstanding this, causing it to shear out. The solution to this problem is distributing the loads by adhering the inner sheet to the flanges, instead of just clamping the inner sheet by the aluminum spars. The failure mode was not seen after this solution was applied, however the number of cycles and tests were limited.

(a) Failure side 1

(b) Failure side 2

Figure 4.6: Failure of the inner sheet due to bearing forces

The 6.7 mil (0.17 mm) thick bellows were tested and although they were not airtight, a continuous supply of air pressure made the bellows inflate, whereas closing the valves slowly let the bellows deflate. The 4 mil (0.10 mm) thick bellows were to be tested as well. However, no test results were created for these bellows. This was caused by the leaks in the bottom. The bond between the first bellow and the aluminum spar was not airtight enough to let the air flow into the bellows, instead the air escaped immediately. Due to the time constraints and the bonding process curing time, it was not possible to get the full test results of the 4 mil thick bellows.

5

TEST RESULTS

The first tests showed that the bottom part of the assembly could not inflate well and therefor did not have any effect on the trailing part. This was caused by the small dimensions of the bellows. Due to time constraints, it was too late to order new parts. Therefor it was chosen to adapt the design with the available materials, the bottom part was replaced by a copy of the top part, resulting in a design as seen in Figure 5.1. This design can not be applied to the 70% chordline in the Cessna Citation inboard flap, but can definitely be used to prove the concept. Then the deflection, deflection speeds, stiffness and damping is measured and described in Sections 5.1 to 5.4 respectively. The tested object is made from bellows with 6.7 mil (0.17 mm) thickness for top and bottom. The first test object has the trailing edge with a 4 mil (0.10 mm) inner sheet. Because of the failure during the deflection rate test, the tests have been performed twice (test 1a and test 1b) for the deflection and the deflection rate test. The second test object had a 6.7 mil (0.17 mm) inner sheet, which is marked as test 2 and is tested for deflection and stiffness. Due to the air tightness issues, the pressure could be varied between deflated, neutral and inflated, where the inflated test required a constant air pressure of 10 psi (0.69 bars) to pressurize the bellows. A third test object has also been produced, using bellows with 4 mil (0.10 mm) thickness. However, for this one the air thightness was so bad, the test results could not be used. To inflate the thinner bellows, less pressure is required as expected, this pressure could be measured since the top bellows had sufficient air tightness. The pressure for the 4 mil bellows was 8.3 psi to inflate, which equals 0.57 bars. Even though it could not be tested, it is expected that any pressure between neutral and inflated, will be an interpolation between both the extremes to determine the deflection, stiffness and damping.

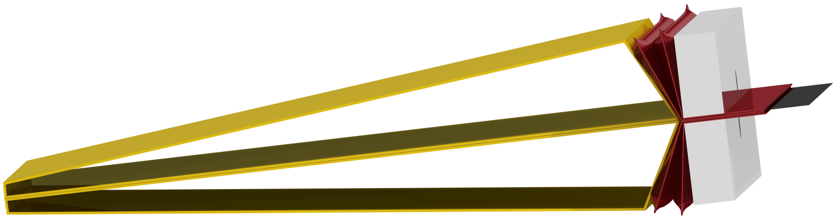

Figure 5.1: Rendering of the test object with the bellows in red, spars in grey, trailing edge in yellow and inner sheet in black

5.1. DEFLECTION

The deflection of the trailing edge has been measured first. The results can be found in Table 5.1. The deflections of test 1a and test 1b can also be found in Figures 5.2a and 5.2b. In Table 5.1 the angles are calculated from the neutral position. The resting position is lower than this neutral position, where test 1a is lower than test 1b and test 2. This is because the trailing edge was spaced closer to the spar for test 1b and test 2. It can be seen that the actuation setup is able to deflect around 17-20 degrees from maximum position at the top to maximum position at the bottom. However, it should be noted that the bellows do not produce a symmetric deflection, where this is expected when the actuator is symmetrical. This can be explained by imperfections in the production and also the gravity pulling the flap down from the 0 degrees position.

Table 5.1: Deflections (Δd) and deflection angles (δ_{morph}) for the deflection tests

	Test 1a		Test 1b		Test 2	
	Δd [mm]	δ_{morph} [deg]	Δd [mm]	δ_{morph} [deg]	Δd [mm]	δ_{morph} [deg]
. Neutral Position	0	0.0	0	0.0	0	0.0
Rest Position	43	11.5	18	5.0	6	1.7
Up Position	-22	-6.0	-21	-5.6	-35	-9.4
Down Position	54	14.4	48	12.8	46	12.4
Both Inflated	25	6.9	24	6.5	38	10.3

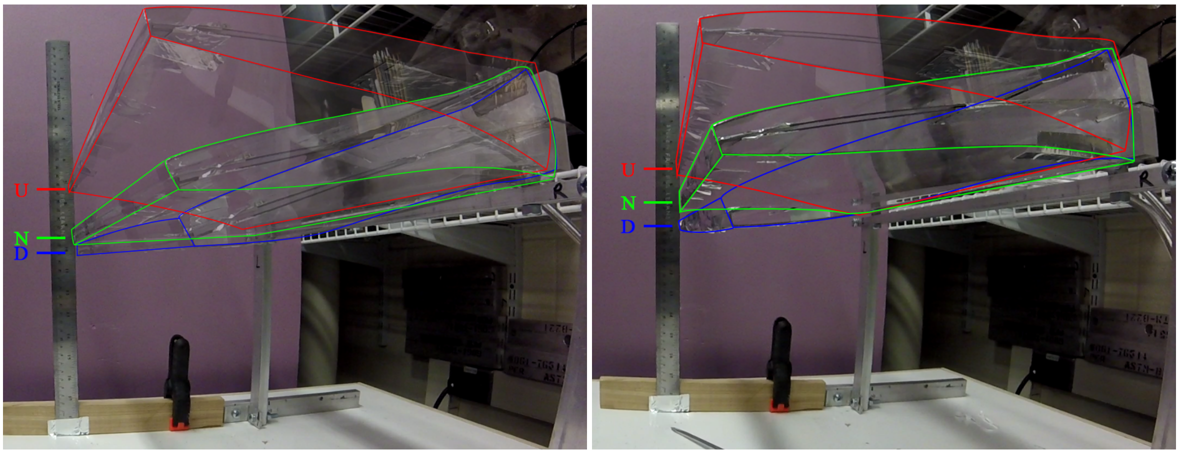

(a) Test 1a

(b) Test 1b

Figure 5.2: Deflection tests with Up (U), Neutral (N) and Down (D) positions

5.2. DEFLECTION RATE

The deflection rate of the actuation system is another important parameter to compare the pressure adaptive bellows to existing actuators. The deflection rate needs to be high enough to enable a fast deflection of the system. When it is too low, the pilot will experience a delay in input and response, which is not desired. Dr. Ron Barrett stated that ailerons have a deflection speed of 1 Hz. He also mentioned that the pilot is able to achieve a maximum input of 2 Hz. The desired actuation speed of the pressure adaptive bellows will be 1 Hz. The actuation system has been tested for the deflection speed, for which the results are given in Figure 5.3a. It can be seen that the deflection overshoots the final state initially. The vibrations between the first overshoot and change in input are not taken into account.

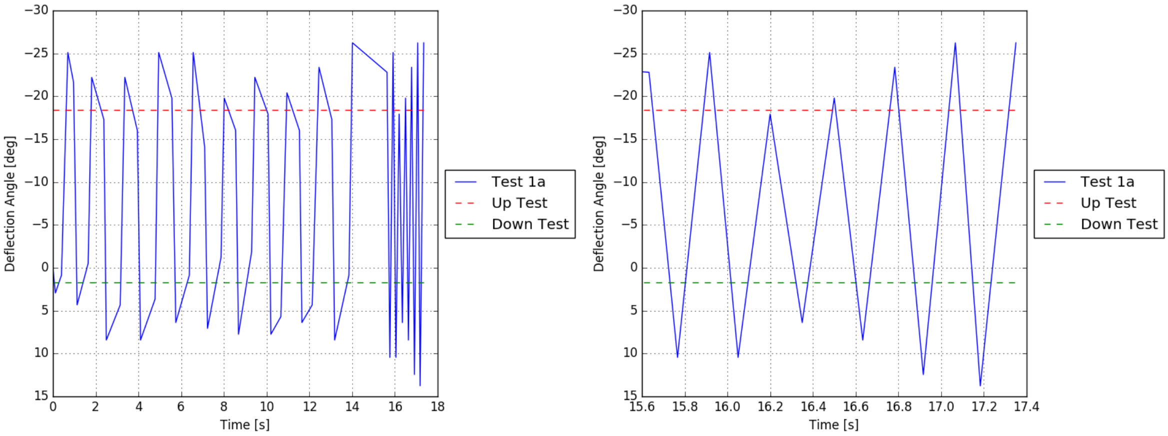

(a) $0 \leq t \leq 18$

(b) $15.6 \leq t \leq 17.4$

Figure 5.3: Deflection speed test 1a, manually sampled with the first deflection peak and the change in input as sample points

In Figure 5.3a it can be seen that in the first 14 seconds, 10 complete deflections are made, which would be a little slower than 1 Hz. From 15.6 seconds till 17.4 seconds a higher rate has been achieved. In Figure 5.3b the graph is zoomed on this part only. In this figure, it can be seen that 6 complete deflections could be made in 1.8 seconds. This is equal to 3.33 Hz. Because the deflections occur so fast the response does not have an overshoot, which was visible in the first part of the test.

The test was repeated, for which the results can be seen in Figure 5.4a. In the first 4.5 seconds, as shown in Figure 5.4b, 5 full cycles have been made (1.11 Hz), whereas between 3.38 and 4.42 seconds the fastest deflection cycles have been measured, where 2 complete cycles can be seen in 1.04 seconds (1.92 Hz). From 10.8 to 17.6 seconds the second series has 6 complete cycles, which is a bit slower, but still 0.88 Hz has been achieved.

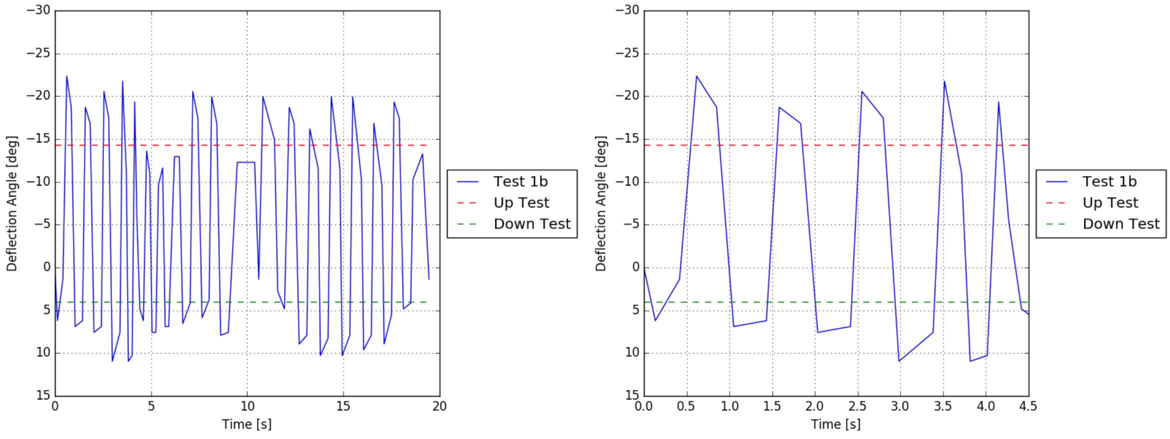

(a) $0 \le t \le 20$

(b) $0 \le t \le 4.5$

Figure 5.4: Deflection speed test 1b, manually sampled with the first deflection peak and the change in input as sample points

The deflection rates have also been determined for these tests. This is shown in Figures 5.5a and 5.5b for test 1a and test 1b respectively. From these figures, it can be seen that the average deflection angular velocities are around 150 deg/s. Which means that if the system performs between +30 and -30 degrees, the system is able to operate at 1.25 Hz for a complete cycle (maximum positive deflection to maximum negative deflection back to maximum positive deflection). This is faster than the current ailerons used in aviation and is sufficient for the pilot's input response.

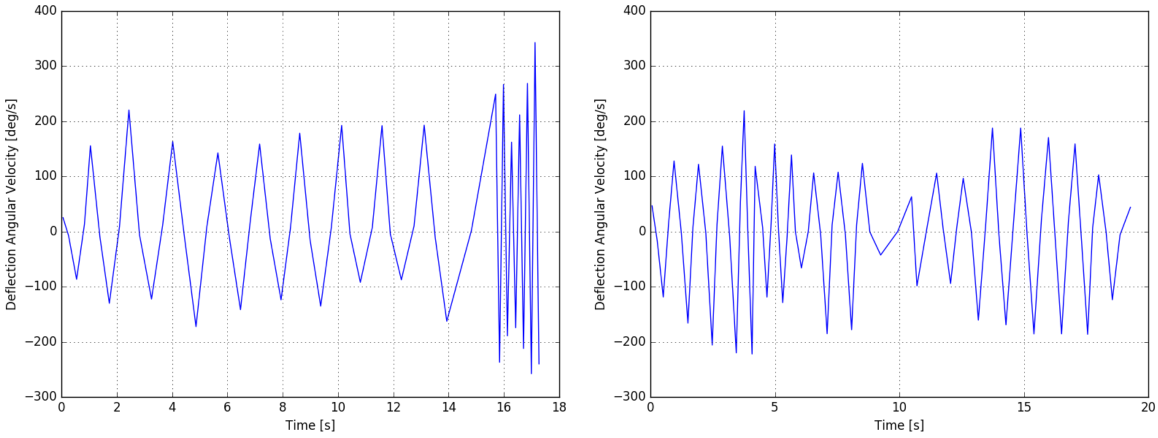

(a) Test 1a

(b) Test 1b

Figure 5.5: Angular velocity for the deflection speed test coming from Figures 5.3 and 5.4

5.3. STIFFNESS

The stiffness of the system is measured by the deflection with different weights under different conditions. For the test the bellows can either be inflated or neutral. This gives 4 different scenarios: top and bottom neutral (Load 1), top inflated and bottom neutral (Load 2), top neutral and bottom inflated (Load 3) and both top and bottom inflated (Load 4). The weights which are being attached are calibrated masses. The following masses are used: 10g, 20g, 50g, 100g, 200g, 500g. With the deflection being measured, the stiffness can be calculated according to Equation (5.1). For this equation, the moment is the weight multiplied with the arm (210 mm). The test setup is given in Figure 5.6a, for which a structural representation is given in Figure 5.6b.

$$\kappa = \frac{M}{\Delta\theta} \tag{5.1}$$

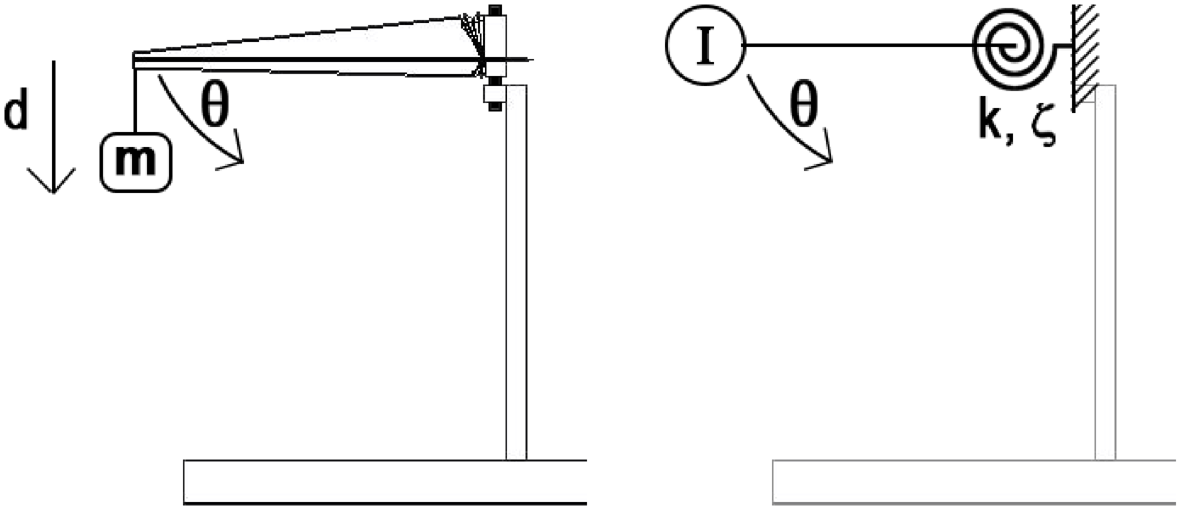

(a) Test model with the location where the weight is attached, indicated position is the neutral position from with deflection d is measured

(b) Structural representation of the test model where the actuator is represented by a spring and the trailing edge with point inertia I

Figure 5.6: Test model and corresponding structural model

The following three data points are collected. The deflections are measured, first without a weight attached. Second with weight attached and third is the possible hysteresis. The test has been performed twice, once with a 4 mil polycarbonate inner sheet, second with a 6.7 mil inner sheet. The first test results can be found in Table 5.2, where the second test results are given in Table 5.3.

Table 5.2: Deflections stiffness test 1b in mm where 1 represents the initial state, 2 the deflected state with weight attached and 3 the hysteresis. Neutral (N) is no pressure supplied and for Inflated (I) 10 psi (0.69 bar) is supplied to the bellows

		Load 1			Load 2			Load 3			Load 4		
	p_{top}/p_{bot}	N/N			I/N			N/I			I/I		
Weight [g]	NP	1	2	3	1	2	3	1	2	3	1	2	3
10	249.2	0.0	1.6	0.0	4.8	6.3	4.8	-55.6	-54.0	-55.6	-20.6	-19.1	-20.6
20	249.2	0.0	3.2	0.0	4.8	6.3	4.8	-55.6	-50.8	-55.6	-20.6	-19.1	-20.6
50	249.2	0.0	7.9	1.6	4.8	7.9	4.8	-55.6	-44.5	-55.6	-20.6	-19.1	-20.6
100	249.2	0.0	11.9	1.6	4.8	14.3	4.8	-55.6	-34.9	-54.0	-20.6	-14.3	-20.6
200	249.2	0.0	27.0	4.8	4.8	27.0	4.8	-55.6	-14.3	-52.4	-20.6	-4.8	-20.6
500	249.2	0.0	63.5	9.5	4.8	68.3	11.1	-55.6	34.9	-46.0	-20.6	36.5	-20.6

Table 5.3: Deflections stiffness test 2 in mm where 1 represents the initial state, 2 the deflected state with weight attached and 3 the hysteresis. Neutral (N) is no pressure supplied and for Inflated (I) 10 psi (0.69 bar) is supplied to the bellows

			Load 1			Load 2			Load 3			Load 4	
	p_{top}/p_{bot}		N/N			I/N			N/I			I/I	
Weight [g]	NP	1	2	3	1	2	3	1	2	3	1	2	3
10	209.6	0.0	1.6	0.0	39.7	41.3	39.7	-41.3	-40.5	-47.6	31.8	33.3	33.3
20	209.6	0.0	1.6	0.0	38.1	38.1	38.1	-20.6	-19.1	-20.6	31.8	33.3	32.5
50	209.6	0.0	22.2	1.6	38.1	41.3	38.1	-17.5	-9.5	-15.9	31.8	33.3	31.8
100	209.6	0.0	11.9	4.8	36.5	41.3	36.5	-19.1	-7.9	-17.5	31.8	36.5	33.3
200	209.6	0.0	22.2	4.8	38.1	46.0	38.1	-15.9	7.9	-13.5	31.8	41.3	33.3
500	209.6	0.0	50.8	6.3	38.1	71.4	42.9	-15.9	42.9	-12.7	33.3	60.3	34.9

The data from Tables 5.2 and 5.3 is presented graphically in Figure 5.7. Figure 5.7a gives the deflections relative to the base, or the neutral point. One remarkable difference between Test 1b (T1) and Test 2 (T2) is the downwards deflections, which are bigger for T2. This difference is mainly caused by the difference in neutral point, which is almost 40 mm. T1 does not have a perfect connection of the trailing edge to the spar, causing the trailing edge to sag down in rest position. Something else which can be seen in this graph is the non linear behavior for the first three weights in most test cases. The data for the heavier weights is more aligned. The slopes for the second test seem to be less negative than the slopes for the first test. This is also shown in Figure 5.7b, where the deflection is normalized, such that the deflection due to the weight is relative to the deflection instead of the neutral point. This graph shows that the slopes, and thus the stiffness, is higher in all load cases in the second test. Looking at the deflection and slope for the third load case (bottom inflated, top neutral), it is noticeable that the deflection and slope are bigger than the first load case (both neutral). This seems counter intuitive, since there are pressure forces restricting downward movement in the third load case. The cause might be in the wedge geometry, where the downward motion is restricted after a certain deflection. The third load case has a bigger deflection before the wedge geometry becomes the limiting factor. In the case the wedge geometry limits the downward movement, the measured stiffness is also coming from the stiffness of the bottom of the trailing edge, which can be seen to deform in Figure 5.8. The wedge is aligned with the spar and the bottom part is under compression forces.

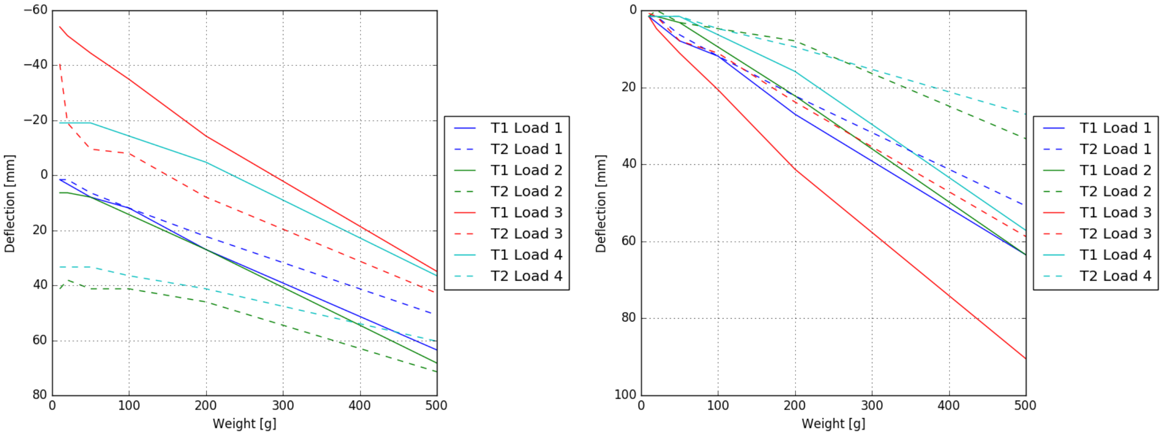

(a) Relative to base

(b) Relative to deflection

Figure 5.7: Stiffness test deflections versus weight for all load cases and both tests (test 1b = T1 & test 2 = T2)

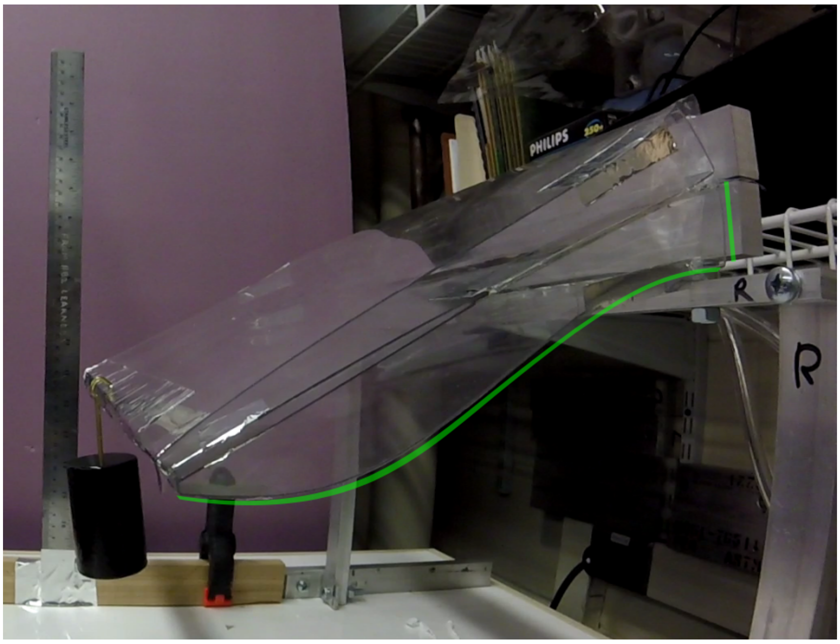

Figure 5.8: Deformation of the bottom part of the trailing edge with the 500 g weight attached

Looking at the hysteresis for the different tests and load cases, it is seen that the hysteresis is negligible for the smallest loads. The hysteresis is the biggest for the neutral load case, as can be seen in Figure 5.9. For the first test, as seen in Figure 5.9a, the hysteresis is over 9 mm for the 500 g weight with the first and third load case. The second load case has 0 mm hysteresis for all weights except 500 g, where it is almost 6.5 mm. The case where both top and bottom bellows are inflated, load 4, shows 0 hysteresis for all weights. In the second test, which is shown in Figure 5.9b, the hysteresis is considerably smaller, except for the case where both bellows are inflated (load 4) and the neutral case for the weights up to 200 g. Similar to the first test, the hysteresis is (almost) constant for load case 4 and it increases for the other load cases up to 500 g. The fact that the hysteresis is small and constant for the fourth load case is beneficial, which means that inflating both bellows can eliminate the hysteresis for the other load cases, when it is subjected to different loads.

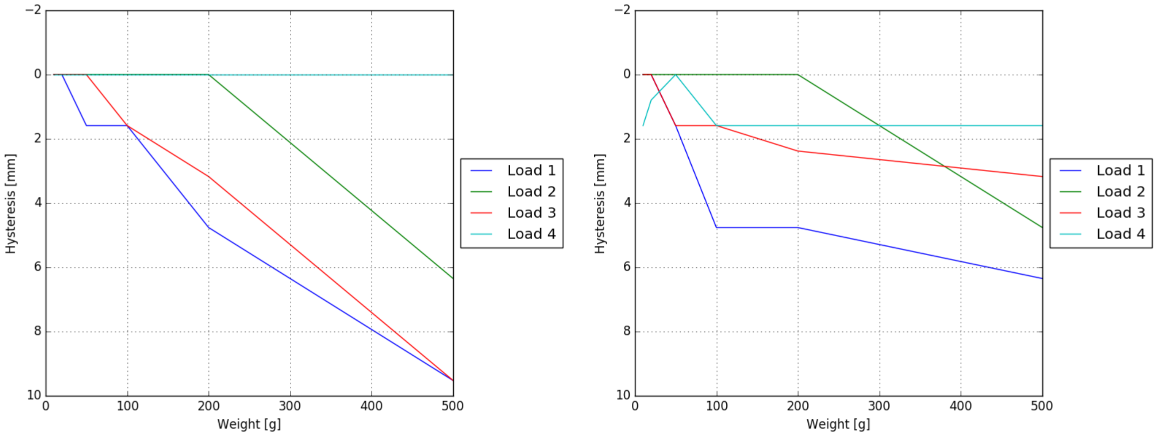

(a) Test 1b (b) Test 2

Figure 5.9: Stiffness test hysteresis versus weight for all load cases

The torsional stiffness calculated for both tests is given in Figures 5.10a and 5.10b. The error bar shows the stiffness range for all load cases and all weights, where the mean is represented by the green bar. It is seen that the stiffness is increased in the second and fourth load case. The second test with the increased thickness of the inner sheet also shows higher stiffness for all the load cases.

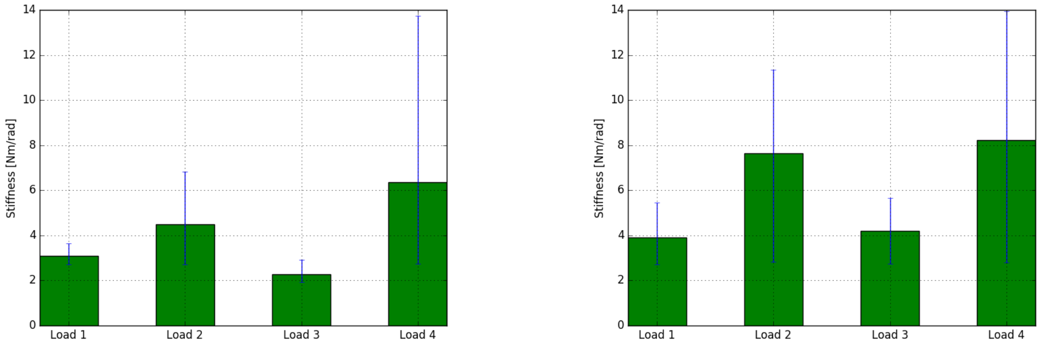

(a) Test 1b

(b) Test 2

Figure 5.10: Equivalent torsional stiffness coefficients for both stiffness tests and all weights included

The error bars in Figures 5.10a and 5.10b are quite big. Since the minimum deflection which is read off is 1/32th of an inch, or 0.79 mm, it is chosen to remove the first 3 weight measurements. The deflection of those measurements are very small, which causes the error bar to increase. The results for removing the first 3 weights is given in Figures 5.11a and 5.11b. The absolute values for all stiffness calculations is found in Table 5.4. If only the higher weights are taken into account for the accuracy of the stiffness test, the stiffness for the neutral case equals 3.46 $N \cdot m/rad$ for the first test and 3.96 $N \cdot m/rad$ for the second test. For the inflated case the stiffness equals 5.38 and 9.03 $N \cdot m/rad$ for the first and second test respectively. Which means that increasing the pressure to 10 psi (0.6895 bar) increases the stiffness with 55.5% and 128.0%. It is expected that the stiffness can be interpolated between the measured points, such that the desired stiffness can be reached within these extremes.

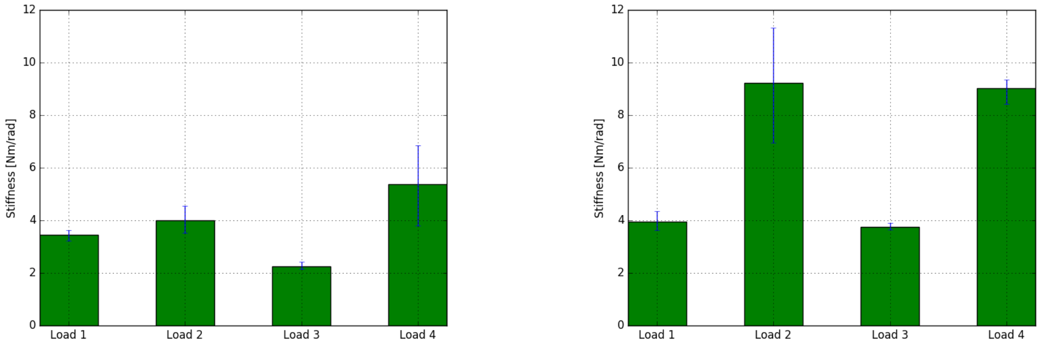

(a) Test 1b

(b) Test 2

Figure 5.11: Equivalent torsional stiffness coefficients for both stiffness tests with weight ranging from 100-500g

Table 5.4: Equivalent torsional stiffness for both stiffness tests in [N · m/rad]

		Test 1b				Test 2			
Weight [g]	Moment [$N \cdot m$]	Load 1	Load 2	Load 3	Load 4	Load 1	Load 2	Load 3	Load 4
10	0.021	2.72	2.73	2.91	2.75	2.72	2.83	5.65	2.79
20	0.041	2.72	5.45	1.93	5.50	5.45	8.24	5.50	5.58
50	0.103	2.73	6.82	2.06	13.74	3.41	7.05	2.74	13.95
100	0.206	3.64	4.55	2.19	6.86	3.64	9.39	3.91	9.32
200	0.412	3.22	3.92	2.16	5.47	3.91	11.34	3.64	9.36
500	1.030	3.51	3.53	2.43	3.81	4.34	6.94	3.72	8.42

5.4. DAMPING

The damping of the system consists of aerodynamic (viscous) damping and spring damping. For the damping tests the following conditions have been tested: neutral, deflated (air being sucked out of the system) and inflated. In Figures 5.12a and 5.12b the results can be found for neutral, deflated and inflated conditions. The response of the system is induced by a deflection. It can be seen that the response damps out faster when there is more air in the system. For the inflated system, this means it damps out after approximately 0.6 seconds, when the initial deflection is approximately 100 mm, the neutral system oscillates twice as long: 1.2 seconds. The deflated system shows the longest response and damps out after 1.6 seconds. The response is a damped sinusoidal motion and is recorded with a 60 frames per second camera. The following points are documented: when the trailing edge reaches a maximum deflection and when the trailing edge passes the neutral deflection line. The graphs in Figures 5.12a and 5.12b represent the numerical interpolation of these points. The time is set to 0 when the trailing edge is released. Especially around this time the interpolation is not perfect since it overshoots the maximum. After 0.1 seconds the interpolation appears to fit the recorded points well as it does not overshoot and forms a nice sinusoidal. Note that in Figure 5.12a the initial deflection is bigger for the deflated test compared to the neutral cases. The angular velocities of the tests corresponding to Figure 5.12 are given in Figure 5.13.

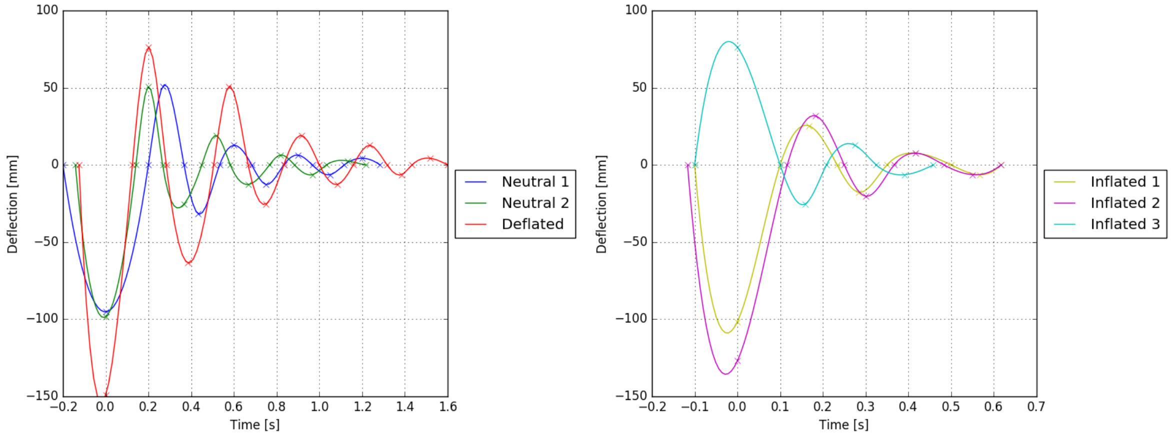

(a) Neutral and deflated test

(b) Inflated test

Figure 5.12: Damping test deflection versus time response for deflated (vacuum) neutral and inflated (10 psi) cases

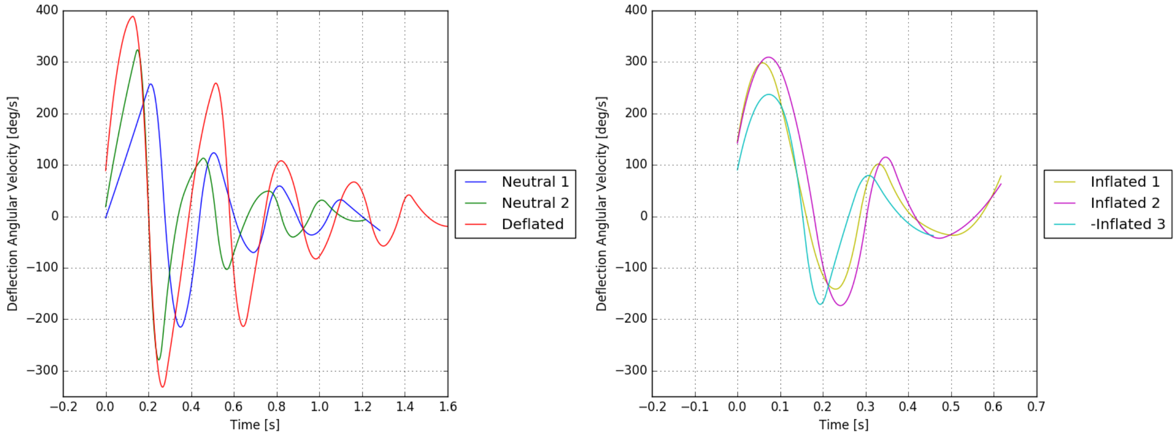

(a) Neutral and deflated test

(b) Inflated test

Figure 5.13: Damping test angular velocity versus time response for deflated (vacuum) neutral and inflated (10 psi) cases

The first peaks in Figure 5.13 after releasing the trailing edge are faster than the manually induced maximum angular velocity. After that, only the deflated test reaches three more peaks with an absolute angular velocity greater than 200 deg/s. Since the graph is a derivative of the interpolation in the deflection points, the graph appears to be less like a sinusoidal. Also, the speed is not 0 at 0 seconds, which is caused by the overshoot in the interpolation. Therefor the first 0.1 seconds in the graph do not have scientific value. From 0.1 seconds to the point where the system is damped, the zero angular velocities line up nicely with the peaks in the deflection. Similarly do the maximum angular velocities line up with the zeroes in the deflection graphs, which is expected for the derivative of a sinusoidal graph.

The damping ratio is then determined according to Equation (5.2). In here, δ is calculated according to Equation (5.3). d_1 and d_2 are two successive maximums.

$$\zeta = \frac{\delta}{\sqrt{(2\pi)^2 + \delta^2}} \tag{5.2}$$

$$\delta = \ln \frac{d_1}{d_2} \tag{5.3}$$

With Equations (5.2) and (5.3) the damping coefficients for all peaks are calculated. The calculated damping coefficients can be found in Figure 5.14. In here the bar represents the average damping coefficient for the test case and the error bar represents the range of all the damping coefficients. T1 and T2 are the neutral tests, T3 is the deflated and T4, T5 and T6 are the inflated tests. Putting more in the bellows will increase the damping coefficient. The damping coefficient for the neutral case is approximately 0.143. The deflated case is 0.119 and the inflated tests ended up having an average damping coefficient of 0.226.

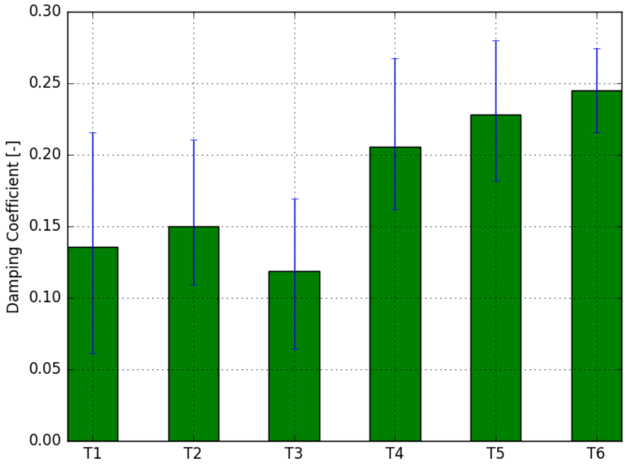

Figure 5.14: Damping coefficients determined from the damping tests, T1 and T2 are neutral, T3 is deflated (vacuum) and T4-T6 are inflated (10 psi)

When looking at the data it is seen that the damping coefficient gradually decreases, when the amplitude decreases. This is shown in Figure 5.15, where the relationship between the absolute maximum velocity between two successive maximum deflections and damping coefficient is analyzed. For both the neutral cases, the damping coefficient decreases with decreasing peak angular velocity. The first neutral case damping coefficient might be influenced by the release, which means that the lower damping coefficient at the highest angular velocity might be erroneous. For the second neutral test, it shows a decreasing damping coefficient, except for the end, where it becomes very irregular and no relationship can be determined. For the deflated case, no relationship can be determined either. The three inflated tests all show a decreasing damping coefficient with decreasing angular velocity. This is expected to be caused by the aerodynamic damping, since the drag forces have a quadratic relation with the speed, the damping will decrease with the speed. Because of the irregular damping for the second neutral case and the deflated case, no such conclusion can be made for these test cases. It should be noted that more damping tests are required to validate the results, before a proper relationship between the speed and damping can be determined. For this reason, the average damping coefficient will be used for the analytic model in Chapter 6.

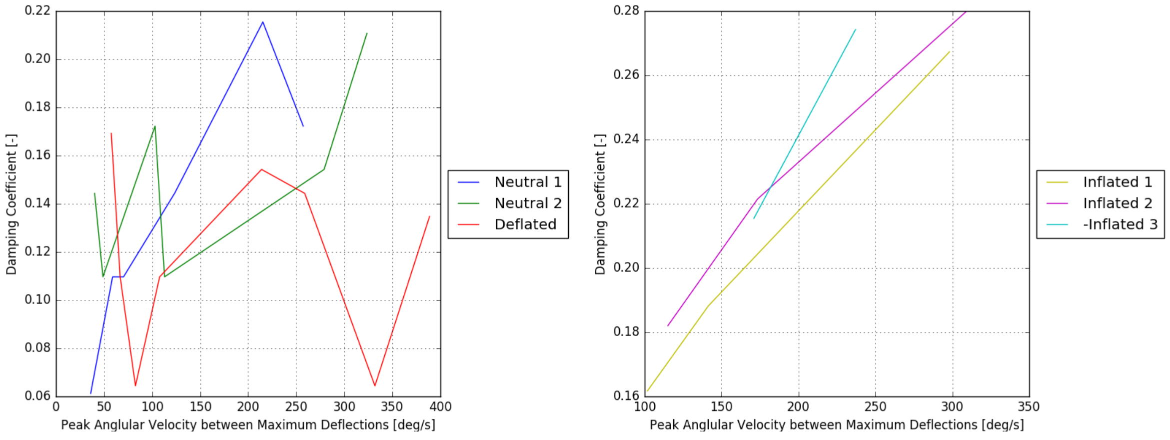

(a) Neutral and deflated test (b) Inflated test

Figure 5.15: Absolute peak angular velocity versus damping coefficient for the damping tests, where neutral is atmospheric pressure, deflated is vacuum and inflated the pressure difference equals 10 psi

From the response given in Figure 5.12, the natural frequency can be calculated. This natural frequency can be used to calculate the stiffness from the dynamic test, which is done with Equation (5.4). The mass moment of inertia in here is determined in CATIA™ and equals 3.468 $\text{g}\cdot\text{m}^2$. The natural frequency and torsional stiffness constant are found in Table 5.5.

$$f_\text{n} = \frac{1}{2\pi}\sqrt{\frac{\kappa}{I}} \tag{5.4}$$

Table 5.5: Natural frequency and torsional stiffness constant calculated from the dynamic tests, where κ is the torsional stiffness calculated with the mass moment of inertia from CATIA™ and κ_2 is calculated with the mass moment of inertia from CATIA™ + 18.7%

Test	f_n [Hz]	κ [N·m/rad]	κ_2 [N·m/rad]
T1	2.92	1.17	1.39
T2	3.08	1.30	1.54
T3	2.97	1.21	1.44
T4	3.65	1.82	2.16
T5	3.65	1.82	2.16
T6	3.82	2.00	2.37

It is seen that the stiffness increases with pressure, however they are a factor 2.9 smaller than the stiffness calculated in the static test. This deficit is partially coming from the mass moment of inertia estimation. In CATIA™, any adhesive is not taken into account, which results in a weight of 278 grams. The measured trailing edge weight equals 330 grams, which is 18.7% more. If the mass moment of inertia increases with 18.7%, the stiffness will increase with the same percentage, however the factor will be reduced from 2.9 to 2.4, which is still a large deficit. This might be caused by inaccuracy of the measurement or the stiffness of the trailing edge. The trailing edge deforms as well, which contributes to the measured stiffness in the static test case. The deflated case (T3) is approximately equal to the neutral cases (T1, T2). It is expected that the stiffness is mainly determined by the inner sheet for these cases, since the bellows do not exert forces on the trailing edge when neutral/deflated.

6

ANALYTIC MODEL FOR STIFFNESS AND DEFLECTION

There are two analytic models, one for the stiffness with differential equations, which is given in Section 6.1. The second model, given in Section 6.2, uses shape functions to predict the deflections which can be achieved.

6.1. STIFFNESS MODEL

The model for stiffness can be seen as a torsional spring damper system. The differential equation for a torsional mass spring damper system is given in Equation (6.1). In this equation, I will be the mass moment of inertia of the morphing part of the wing, ζ the damping coefficient and k the torsional stiffness. The left hand side, τ, is the externally applied torque.

$$\tau = I\ddot{\theta} + \zeta(\Delta p)\dot{\theta} + \kappa(\Delta p)\theta \tag{6.1}$$

Since there are multiple factors contributing to the stiffness and damping, the coefficients are hard to be determined. In literature, there is no model for the pressure adaptive bellows available. Since the damping coefficient is also build up from viscous damping and spring damping, the system will become very complex to solve analytically. It is chosen to have the coefficient being determined by testing because of this complexity. The empirical data for the damping coefficient and stiffness constant is determined by the tests in this thesis and can be found in Table 6.1. In this table, the mass moment of inertia, I, is determined by CATIA™. What can be seen is that some of the cells are still empty, marked with n/a, because these tests are not performed yet. However the static stifness cases can be seen for both tests in neutral and inflated condition, where test 1 has the thinner, 4 mil (0.10 mm) inner sheet and test 2 the 6.7 mil (0.17 mm) inner sheet. The stiffness and damping are functions of the pressure. The exact shape of these functions could not be determined. For now it is assumed that any change in pressure will be a linear interpolation between the known points.

Table 6.1: Empirically determined constants and coefficients for the torsional spring damper system as given in Equation (6.1), where κ is the torsional stiffness calculated with the mass moment of inertia from CATIA™ and κ_2 is calculated with the mass moment of inertia from CATIA™ + 18.7%

Coefficent	Unit	Test 1			Test 2		
State		Deflated	Neutral	Inflated	Deflated	Neutral	Inflated
Δp	psi	-14.7	0.0	10.0	-14.7	0.0	10.0
I	$g \cdot m^2$		3.468			3.556	
ζ		0.119	0.143	0.226	n/a	n/a	n/a
κ_{static}	$N \cdot m/rad$	n/a	3.46	5.38	n/a	3.96	9.03
κ_{dynamic}	$N \cdot m/rad$	1.21	1.24	1.88	n/a	n/a	n/a
$\kappa_{\text{dynamic,2}}$	$N \cdot m/rad$	1.44	1.47	2.23	n/a	n/a	n/a

The model can be validated by producing the time response to an initial deflection ($\theta(0) \neq 0$) and comparing the results to Figure 5.12. This is done with the first test results from Table 6.1, since the damping test is performed with the 4 mil inner sheet. The validation has been performed with the stiffness from the dynamic test. For the mass mass moment of inertia, an increase of 18.7% of the CATIA™ is assumed, because the measured mass is 18.7% higher than the mass coming from CATIA™. This increase, together with the dynamic test stiffness, gives a more accurate representation of the frequency of the response. The results of the validations is given in Figure 6.1.

Considering the frequency for the neutral cases in Figure 6.1a, the peaks from the model are leading the test results for the first neutral test up till the end of the measurement. For the second neutral test the model is leading till approximately 0.65 seconds. The model is leading till 1.4 seconds in the deflated case. A similar result is found in the inflated cases, as seen in Figure 6.1b, where it is leading till approximately 0.4 seconds for the first two inflated cases. The third inflated case is leading up till approximately 0.2 seconds. This means the frequency is a little underestimated in the model and the response should be a little delayed. This can be caused by the measurement inaccuracy and because the equivalent, dynamic torsional stiffness is taken from the average frequency of the complete response. The delay might be necessary because the response might still be influenced by the release at 0 seconds. If the delay is added the response would overlap more in the first couple of peaks.

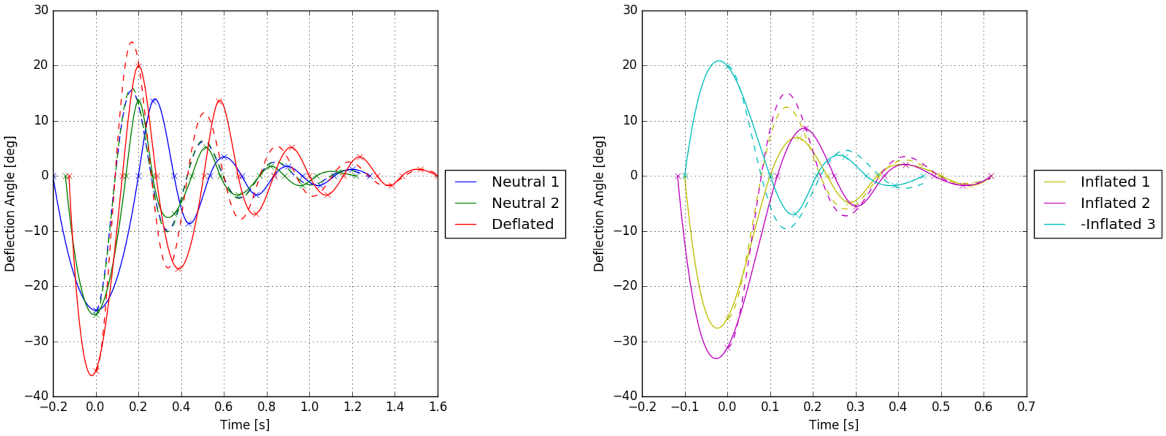

(a) Neutral and deflated test

(b) Inflated test

Figure 6.1: Validation of the coefficients, as given in Table 6.1, for the torsional spring damper system from Equation (6.1) where the dotted line represents the model and the solid lines are the test results

Considering the damping, the first peaks are higher in the model than the tests. The biggest overshoot is found in the second inflated case. After the first peak, the damping in the model gives a much better representation of the test results as the amplitudes of the peaks are almost equal. The difference might be explained by the assumption of taking the mean in the damping coefficient tests, where the damping coefficient in the test decreases with decreasing peak amplitude. This decrease in the peak amplitude makes the angular velocity decreases as well, which lowers the viscous damping part. This can be solved by making the damping coefficient a function of the velocity, if such relation exists.

6.2. DEFLECTION MODEL

For the deflection analytic model of a single bellow a couple assumptions have to be made:

1. The bellows are thin walled.
2. The pressurized bellow is an (super) ellipse with the width being 30% of the height.
3. The contact point of the bellow and the trailing edge/adjacent bellow is the thickest point.
4. Neutral state is ellipse on the top halve and super-ellipse on the bottom halve with $N = 1.1$.

The first assumption states that the bellows thickness is a lot smaller than all other dimensions. The thickest bellow measures 6.7 mil (0.17 mm) in thickness. The bottom bellows are about 9.5 mm in height, such that the thickness is less than 2% of the height. Due to the connection of the bellow to the stringer, the close-outs and the bottom of the bellows, the bellows are restricted to become spheres/cylinders. Therefor it is chosen to approximate the pressurized bellow as ellipse, with $a \leq 0.3b$, and a being the horizontal ellipse parameter. It is chosen that the thickest point is the contact point as well, this simplifies the model and the contact point will be approximately at that location. The circumference of the final ellipse is calculated with Equations (6.2) and (6.3) according to Ramanujan [34]. Using assumption 2, it is easy to determine b, after which a and the final angle can be determined. The deflection is assumed to be the difference between the initial and the final angle. For a single top bellow structure, the difference between initial and final angle equals 17.43 degrees, the bottom bellow will have an angle difference of 5.87 degrees.

$$\text{circumference} \approx \pi(a+b)\left(1+\frac{3\lambda^2}{10+\sqrt{(4-3\lambda^2)}}\right) \tag{6.2}$$

$$\lambda = \frac{(a-b)^2}{(a+b)^2} \tag{6.3}$$

The multibellow is more complex because of the attachment point. The bellow bottom is assumed to be still super-elliptical. The final shape is approximated by computing the arc length of the super-ellipse and the ellipse. The circumference has to be constant, however there are four variables in the equation: a, b_{bot}, b_{top} and N, where b_{bot} is the height of the bottom super-ellipse and b_{top} is the height of the top super-ellipse. The number of bellows will also effect the N-factor. The best approach would be analyzing the shape of the inflated bellow, comparing these shapes with the shapes generated with the various parameters and then determining the angle. The model is given in Figures 6.2 and 6.3. The bellows seem to deform to the green shapes from Figure 6.3d, with N between 1.5 and 2. From Figure 6.3b the final angle for these shapes is approximately 22 degrees. Subtracting the initial angle (16 degrees) leads to a deflection of 6 degrees per bellow, which means that a 2-bellow structure will be able to deflect 12 degrees up and down. During testing, a deflection range was found of 20.4 degrees, which is a bit smaller than the expected 24 degrees. This might be because of imperfections in production, the bellow interaction is not correctly modeled, the shape is not uniform across the complete span or the shapes do not completely match.

It is less likely that the bellows will end up in the red and blue shapes from Figures 6.2d, 6.3c and 6.3d. If the manufacturing imperfections are improved, the bellows might end up to shapes like the ones given in Figure 6.2c. These shapes have a larger angle as seen in Figure 6.2a and will be able to induce bigger deflections.

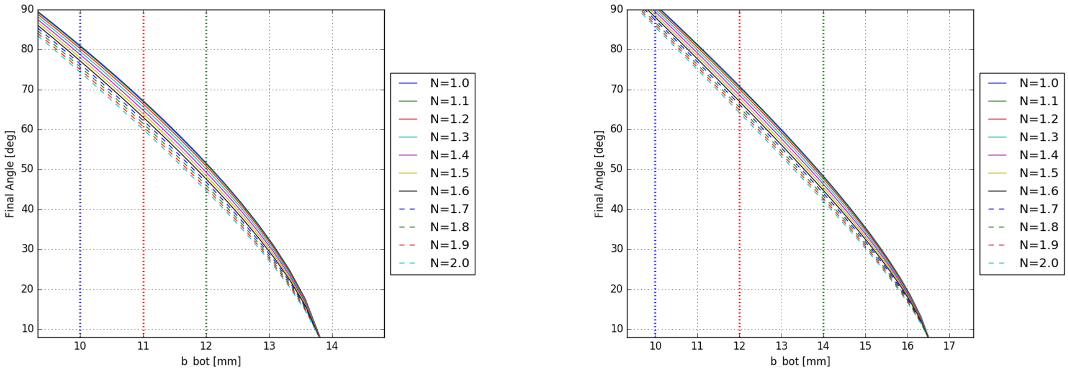

(a) Angle $\frac{b_{\text{bot}}}{b_{\text{top}}} = 1$

(b) Angle $\frac{b_{\text{bot}}}{b_{\text{top}}} = 1.5$

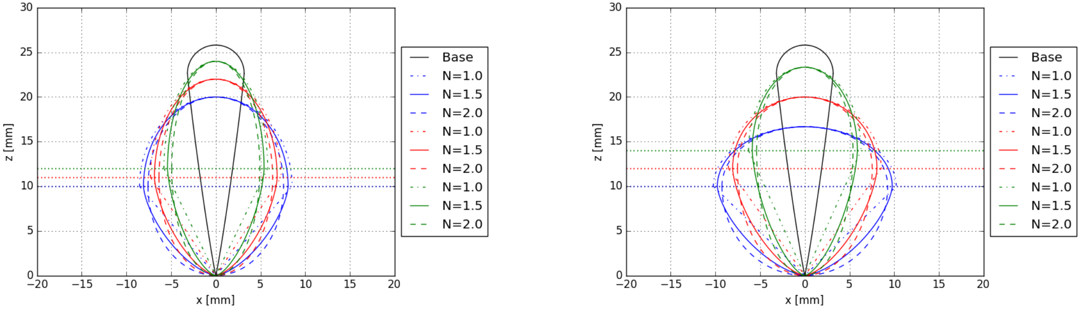

(c) Shape $\frac{b_{\text{bot}}}{b_{\text{top}}} = 1$

(d) Shape $\frac{b_{\text{bot}}}{b_{\text{top}}} = 1.5$

Figure 6.2: Final angle for a single bellow with different parameters and the corresponding shapes for $\frac{b_{\text{bot}}}{b_{\text{top}}} = 1$ and $\frac{b_{\text{bot}}}{b_{\text{top}}} = 1.5$

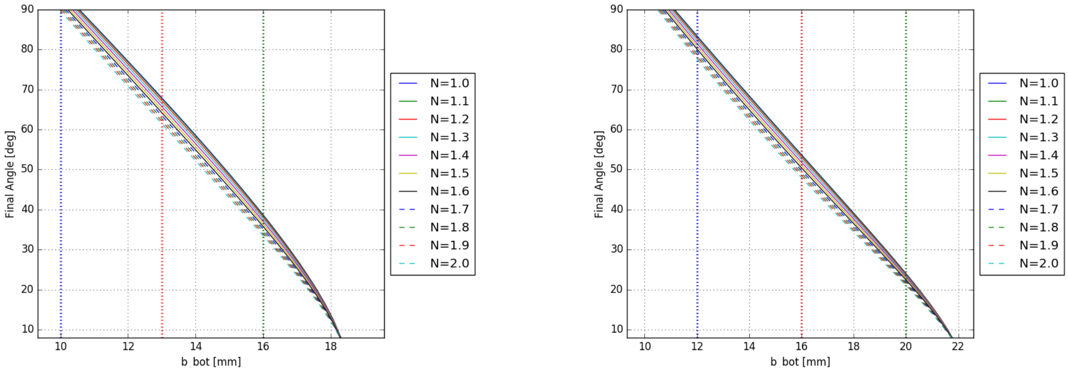

(a) Angle $\frac{b_{\text{bot}}}{b_{\text{top}}} = 2$

(b) Angle $\frac{b_{\text{bot}}}{b_{\text{top}}} = 4$

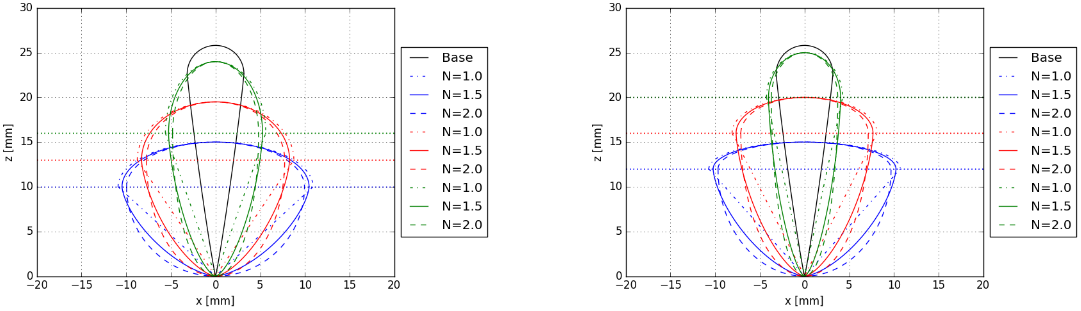

(c) Shape $\frac{b_{\text{bot}}}{b_{\text{top}}} = 2$

(d) Shape $\frac{b_{\text{bot}}}{b_{\text{top}}} = 4$

Figure 6.3: Final angle for a single bellow with different parameters and the corresponding shapes for $\frac{b_{\text{bot}}}{b_{\text{top}}} = 2$ and $\frac{b_{\text{bot}}}{b_{\text{top}}} = 4$

7

CONCLUSIONS AND RECOMMENDATIONS

The Cessna Citation X inboard flap is measured and modeled in this thesis. The main focus was on producing an actuator to achieve variable camber and stiffness and testing the structural behavior of a pressure adaptive trailing edge. The answers to the research questions are found in Section 7.1. During the production and testing phase of the actuator, recommendations for improvements and further research were found, which are given in Section 7.2.

7.1. CONCLUSIONS TO SUB RESEARCH QUESTIONS

The first main research question is focused on the design and manufacturability of a full scale business jet inboard flap with a pressure adaptive trailing edge. The flap is coming from an existing airplane, which means that the application of the pressure adaptive trailing edge requires some adaptations to the current structure. The current flap structure consists of a load carrying skin, build from graphite composites and a Kevlar® coating. The 30% of the trailing edge will be replaced with the actuator. The front part of the flap will change in a D-spar, where stringers will be placed on the 70% chordline from the leading edge. The actuator can be attached to the stringers, which makes the adaptations minor. The flap is split in five separate actuators in spanwise direction.

The width of a single actuator will be 334 mm. The actuator will consist of two bellows for top and bottom, two L-shaped stringers, a flexible inner sheet and a trailing edge top and bottom with a wedge geometry at the pivot location. The bellows and the trailing edge will be made of polycarbonate, a flexible polymer with relatively high strength properties. The actuator itself is not optimized for weight yet, however a weight estimation has been made. A single actuator will have a weight of 475 grams, which means the flap weight will be increased by 2375 grams. The estimated weight for the flap without tracks equals 12345 grams, which makes the flap weight increase with 18.9% when the actuators are installed.

The closeout of the bellows can be done by applying adhesive. Since the air tightness is determined by the weakest bond in the actuator, the closeout has to be strong enough to withstand the pressure forces. It is expected that the closeout of the bellows and the bond between the spar and the bellows will be the weak links. This is because any volume under pressure will have the tendency to become spheres, the closeout and attachment will restrict this behavior. Since the bellows could not be made fully airtight, the closeout problem is not solved yet. To fully answer this question, the location of the leak(s) has to be determined.

The design of the bellows and actuator is initially made in two dimensions. The actuator will be three dimensional, which means that the spanwise direction has to be added to the design. This includes the closeout, but also the curvature of the flap, taper ratio and thickness distributions. The dihedral of the flap is following the dihedral of the wing root, such that the root of the flap is curved. The 70% chord line is pretty straight with only some dihedral effects. Splitting up the trailing edge into five segments allows to follow the dihedral of the flap well. The flap itself is not tapered, only the wing is tapered at this location. The thickness distribution will change in the spanwise direction, where the root is thicker than the tip of the flap. This means that the actuator will have more space at the root compared to the tip. The presented design will fit in the middle of the flap, the other actuators can be derived from this design, adjusted to the available height.

The optimal wedge geometry consists of a couple parameters: the height of the top and bottom part of the wedge and the angles of the wedge. The height ratio is determined from the expected loading. The moment ranges from -12.68 N·m to 37.19 N·m, where a negative moment means a downwards rotating moment. The forces range from -253.4 N to 631.6 N, where downforce is negative. This is a ratio of approximately 1:3 for the moments and 1:2.5 for the forces. The height ratio will be between 1:2.5 to 1:3, determined from a preliminary loading estimation. The bellows are designed with the ratio of maximum positive load factor to the maximum negative load factor, which is 1:2.62, which fits in the previously suggested range.

The wedge angle is determined from the minimum deflection or the bellow contact requirement. The design will be optimal if the minimum deflection requirement drives the wedge angle. The angle has to be at least 15 degrees if the minimum desired deflection is 15 degrees. If the contact between the bellows and trailing edge is reduced by this angle, another bellow can be added to fulfill this requirement.

When the implications for production are solved and the actuator is actually produced, it can be tested. The second main research question focused on the structural properties of the pressure adaptive trailing edge, which could be determined by bench testing the full scale flap. Because the bench tests of the full scale flap are not performed, conclusions are made on the structural properties of a single actuator.

From the static stiffness tests, the stiffness increases from 3.46 to 5.38 N·m/rad with a 4 mil (0.10 mm) thickness inner sheet and increases from 3.96 to 9.03 N·m/rad for the 6.7 mil (0.17 mm) inner sheet. From the dynamic tests, the stiffness is lower, but increases as well with increasing air pressure: 1.24 N·m/rad for neutral bellows and 1.88 N·m/rad for inflated bellows. The increase is coming from the pressure in the bellows, which are inflated from neutral to 10 psi (0.6895 bar). The damping also increased with increasing pressure, where deflated the damping coefficient was equal to 0.119, neutral 0.143 and inflated at 10 psi the damping coefficient equals 0.226. Together with the mass moment of inertia, equal to 3.468 $g \cdot m^2$ for the 4 mil inner sheet and 3.556 $\mathrm{g \cdot m^2}$ for the 6.7 mil inner sheet, the coefficients for a torsional spring damper system are determined.

To determine whether the bellow structure will be stiff enough to withstand the loads, stiffness tests have been performed. With weights ranging from 10 - 500 g a moment is induced (ranging from 0.021 - 1.030 N·m) and the stiffness can be determined by the deflection. The tested loads are a lot smaller than the expected loads on the actuator, however the actuator is not able to keep the trailing edge neutral with the highest applied load, which means it is not stiff enough for the design loads in the current design.

The deflections achieved by the actuator, range from 13 degrees upwards and 7 degrees downwards. This can also be modeled by analyzing the deformations of the bellows while inflating them, after which the deflection angle can be calculated. The deflection speed averages about 150 deg/s and deflection rates of 3.33 Hz are achieved.

The functionality of the actuator can be both variable camber and variable stiffness. Variable camper will only have a minor impact, since it will only affect a small area of the wing. The variable stiffness may have a bigger impact, especially for gust load alleviation by changes in lift coefficient gradient. To apply the concept and use the variable stiffness in aircraft designs, recommendations on further research are given.

7.2. RECOMMENDATIONS ON FURTHER RESEARCH

The presented actuator shows promising results and proved the possibility to apply variable stiffness and camber to the trailing edge of the wing. However, the results are coming from a limited amount of tests, in which still some issues were found. In these limited number of tests, the loads used for measuring the stiffness do not represent the loads experienced during flight. To make more appropriate conclusions on the stiffness, the tested loads need to be a better representation of the expected loads and moments.

The highest tested load was already putting the actuator to its limits. Therefor it is recommended to increase the stiffness of the inner sheet. It is seen that increasing the thickness from 4 mil (0.10 mm) to 6.7 mil (0.17

mm) already increased the stiffness of the actuator. There will most likely be a thickness fulfilling the stiffness requirement.

As experiment, the hole through the spar supplying the air pressure to the bellows, was tapered. Tapering the hole did not limit the air supply to the bellows, however it gave more surface for the adhesive and simplified the assembly process. A smaller and or tapered hole is recommended to use, which can be achieved by using tubes with a smaller diameter. The air tightness can probably also be increased by using a different adhesive instead of acrylics. It is expected that the acrylics is the weak bond in the bellows. However to fully conclude on this, the source of the leaks will have to be determined.

Currently it is seen that with the heavier weights, the maximum deflection of the actuator is reached and even exceeded. The trailing edge was able to deflect further downwards, since the trailing edge was flexible. This might have caused some erroneous data in the stiffness tests with the top bellows inflated. It is suggested to use a material with higher stiffness, to prevent any further deflections, which limits the chances of erroneous data. The trailing edge can also be integrated with the trailing edge skin, build from graphite composites and Kevlar® coating.

Since the damping test has only been performed for the 4 mil inner sheet and the test could not be performed with the 4 mil bellows, it is recommended to perform tests with these parts to find the missing data. Besides the thicknesses used for testing, more objects with different thickness should be used to study the effect of thickness on the coefficients as well. Repetition of the same test is advised, the coefficients and results are currently based on a single test, which means that outliers can contaminate the results. These outliers can be caused by various reasons, coming from either manufacturing, testing or read-off errors. Once more empirical data is available, the model can be improved and updated.

To get the concept certified and ready to use, it has to be adapted to the regulations as well. Just by simply using the materials from the FAR-databases, does not mean it is certifiable. According to FAA manager Wes Ryan, from the programs & procedures (advanced technology) department, a couple challenges still need to be tackled. He identified the main concerns to be asymmetric deployment, inadvertent deployment above the tested flap speeds, inappropriate or commanded deployment, structural failure and the reliability and integrity of the systems that control and prevent all the aforementioned concerns. The system also needs to indicate the positioning to the pilot and the effects of high intensity radiation fields and lightning to the actuator still need to be addressed. The behavior of the flap needs to be investigated in a combined aerodynamic and structural method.

The concept has proven to achieve both variable camber and variable stiffness with a preliminary design. The results look promising and can improve the aircraft efficiency and ride quality. But before the concept can actually be integrated in aircraft, more testing on multiple test objects will be necessary.

BIBLIOGRAPHY

[1] A M O Smith. High-Lift Aerodynamics. *AIAA Journal*, 12(6), dec 1974.

[2] Daniel Reckzeh. Aerodynamic design of Airbus high-lift wings in a multidisciplinary environment. *Eccomas*, pages 1–19, July 2004.

[3] Sridhar Kota, Russell Osborn, Gregory Ervin, Dragan Maric, Peter Flick, and Donald Paul. Mission Adaptive Compliant Wing – Design , Fabrication and Flight Test Mission Adaptive Compliant Wing. In *RTO Applied Vehicle Technology Panel (AVT) Symposium*, pages 1–19, 2009.

[4] J. Szodruch and R. Hilbig. Variable wing camber for transport aircraft. *Progress in Aerospace Sciences*, 25(3):297–328, 1988.

[5] Alexander Bolonkin and Glenn B. Gilyard. Estimated Benefits of Variable-Geometry Wing Camber Control for Transport Aircraft. *Nasa/Tm-1999-206586*, October 1999.

[6] Fred Austin, Michael J Siclari, William Van Nostrand, G Nick Weisensel, Vishnu Kottamasu, and Giuseppe Volpe. Comparison of smart-wing concepts for transonic cruise drag reduction. *Smart Structures and Materials*, 3044:33–40, 1997.

[7] H P Monner, D Sachau, and E Breitbach. Design Aspects of the Elastic Trailing Edge for an Adaptive Wing. In *Structural Aspects of Flexible Aircraft Control*, 1999.

[8] B K S Woods and M I Friswell. Preliminary Investigation of a Fishbone Active Camber Concept. In *Smart Materials, Adaptive Structures and Intelligent Systems*, sep 2012.

[9] Senthil Murugan, B. K S Woods, and M. I. Friswell. Hierarchical modeling and optimization of camber morphing airfoil. *Aerospace Science and Technology*, 42:31–38, 2015.

[10] J. H S Fincham and M. I. Friswell. Aerodynamic optimisation of a camber morphing aerofoil. *Aerospace Science and Technology*, 43:245–255, 2015.

[11] Michael Sinapius, Hans Peter Monner, Markus Kintscher, and Johannes Riemenschneider. DLR's morphing wing activities within the European network. *Procedia IUTAM*, 10:416–426, 2013.

[12] N Di Matteo, S Guo, and D Li. Morphing Trailing Edge Flap for High Lift Wing. In *Structures, Structural Dynamics and Materials Conference*, pages 1–13, April 2011.

[13] Jonathan D. Bartley-Cho, Donny P. Wang, Christopher A. Martin, Jayanth N. Kudva, and Mark N. West. Development of High-rate, Adaptive Trailing Edge Control Surface for the Smart Wing Phase 2 Wind Tunnel Model. *Journal of Intelligent Materials Systems and Structures*, 15(4):279–291, 2004.

[14] A.Y.N. Sofla, D.M. Elzey, and H.N.G. Wadley. Two-way Antagonistic Shape Actuation Based on the One-way Shape Memory Effect. *Journal of Intelligent Material Systems and Structures*, 19(9):1017–1027, 2008.

[15] B Berton. Shape Memory Alloys Application: Trailing Edge Shape Control. *Multifunctional Structures / Integration of Sensors and Antennas*, 13, 2006.

[16] Sm Yang, Jh Han, and In Lee. Characteristics of smart composite wing with SMA actuators and optical fiber sensors. *International Journal of Applied Electromagnetics and Mechanics*, 23:177–186, 2006.

[17] Liu Shili, Ge Wenjie, and Li Shujun. Optimal Design of Compliant Trailing Edge for Shape Changing. *Chinese Journal of Aeronautics*, 21(2):187–192, 2008.

[18] Sahng Min Lim, Lee Sangki, Hoon Cheol Park, Kwang Joon Yoon, and Nam Seo Goo. Design and demonstration of a biomimetic wing section using a lightweight piezo-composite actuator (LIPCA). *Smart Materials and Structures*, 14, 2005.

[19] Sebastian Heinze and Moti Karpel. Analysis and Wind Tunnel Testing of a Piezoelectric Tab for Aeroelastic Control Applications. *Journal of Aircraft*, 43(6):1799–1804, nov 2006.

[20] Roelof Vos, Ron Barrett, Roeland de Breuker, and Paolo Tiso. Post-buckled precompressed elements: a new class of control actuators for morphing wing UAVs. *Smart Materials and Structures*, 16(3):919, 2007.

[21] Roelof Vos. *Mechanics and applications of pressure adaptive honeycomb*. PhD thesis, The University of Kansas, 2009.

[22] Roelof Vos and Ron Barrett. Pressure Adaptive Honeycomb: Mechanics, Modeling, and Experimental Investigation. *Structures, Structural Dynamics and Materials Conference*, 2010.

[23] Roelof Vos and Ron M. Barrett. Pressure Adaptive Honeycomb: a Novel Concept for Morphing Aircraft Structures. 2010.

[24] Roelof Vos, Ron Barrett, and Albert Romkes. Mechanics of Pressure-Adaptive Honeycomb. *Intelligent Material Systems and Structures*, 2011.

[25] Roelof Vos, Jan Scheepstra, and Ron Barrett. Topology Design of Pressure Adaptive Honeycomb for a Morphing Fowler Flap. *52nd AIAA/ASME/ASCE/AHS/ASC Structures, Structural Dynamics and Materials Conference*, 3(1):1–5, 2011.

[26] Roelof Vos and Ron Barrett. Mechanics of Pressure-Adaptive Honeycomb and its Application to Wing Morphing. *Smart Materials and Structures*, 20, jul 2011.

[27] Christopher D Regan and Christine V Jutte. Survey of Applications of Active Control Technology for Gust Alleviation and New Challenges for Lighter-weight Aircraft. Technical Report TM-2012-216008, NASA, 2012.

[28] Ronald M Barrett and Cassandra M Barrett. Biomimetic FAA-certifiable, artificial muscle structures for commercial aircraft wings. *Smart Materials and Structures*, (23), apr 2014.

[29] Ihs. Jane's All the World's Aircraft: Cessna 750 Citation X. `https://janes.ihs.com/JAWADevelopmentProduction/Display/1343275`, 2016.

[30] FlightGlobal. Cessna Citation Excel Cutaway Poster. `http://www.flightglobalimages.com/cessna-citation-excel-cutaway-poster/print/1571089.html`.

[31] David Lednicer. The Incomplete Guide to Airfoil Usage. `http://m-selig.ae.illinois.edu/ads/aircraft.html`, 2010.

[32] Dr. Jan Roskam. *Airplane Design Part V: Component Weight Estimation*. DARcorporation, Lawrence, KS, 2003.

[33] William D. Callister and David G. Rethwisch. *Materials Science and Engineering*. John Wiley & Sons, Inc., 2011.

[34] John D. Cook. Ramanujan approximation for circumference of an ellipse. `https://www.johndcook.com/blog/2013/05/05/ramanujan-circumference-ellipse/`, 2013.